Evidence for polybaric fractional crystallization in a continental arc: Hidden Lakes mafic complex, Sierra Nevada batholith, California

Evidence for polybaric fractional crystallization in a continental arc: Hidden Lakes mafic complex, Sierra Nevada batholith, California

Evidence for polybaric fractional crystallization in a continental arc: Hidden Lakes mafic complex, Sierra Nevada batholith, California

Madeline J. Lewis*[1], Claire E. Bucholz[1], Oliver E. Jagoutz[2]

1. Division of Geological and Planetary Sciences, California Institute of Technology
2. Department of Earth, Atmospheric, and Planetary Sciences, Massachusetts Institute of Technology

*Correspoding Author: Madeline J. Lewis, maddie@purdue.edu

ABSTRACT

Although the voluminous granitoids that constitute the upper crust of the Sierra Nevada batholith (California) have been investigated in detail, comparatively few studies focus on the origin of mafic bodies at similar crustal levels. Here, we present field and petrographic observations, geochronology, and geochemistry of the Hidden Lakes mafic complex in the central-eastern Sierra Nevada batholith. Our results show that the complex comprises norites, gabbros, monzondiorites, and monzonites that record fractional crystallization of a hydrous (~3 wt.% H_2O), non-primitive basalt within the upper crust (0.3 GPa) at c. 95-96 Ma. To quantitatively model the generation of the observed lithologies, we construct a two-stage polybaric crystallization model based on cumulate and melt-like bulk-rock compositions. In the first step, we model fractionation of a primitive, mantle-derived basalt at >30 km depth, generating dominantly

pyroxenite cumulates. The evolution of the derivative melt (67% of melt mass remaining) is then modeled to fractionate at 12 km depth to produce the observed lithologies within the Hidden Lakes mafic complex. Extension of this model to higher-silica melt compositions (>65 wt.% SiO_2) replicates observed granodiorite compositions in the batholith, suggesting that polybaric crystallization could be an important process for the generation of arc granitoid melts. The depth of differentiation in continental arcs is debated, as field observations indicate abundant lower crustal fractionation while experimental data suggests that high-pressure crystallization of hydrous basalts cannot produce the non-peraluminous granitoid compositions observed in continental arc batholiths. Our model supports polybaric differentiation as one potential mechanism to resolve this inconsistency.

Introduction

The generation of batholith-scale granodiorite intrusions in continental arc settings is an unresolved problem, as differentiation mechanisms produce only small volumes of granitic melt (~10-20% of original melt mass) in comparison to much greater volumes of ultramafic and mafic cumulates or restites (Kay and Kay 1985; Soesoo 2000; Jagoutz and Klein 2018). However, lower crustal mafic and ultramafic cumulates are ubiquitous in magmatic arcs exhumed to 30 to 55 km depths (Debari and Sleep 1991; Greene et al. 2006; Jagoutz et al. 2009; Jagoutz 2010; Otamendi et al. 2012; Jagoutz 2014; Walker et al. 2015; Guo et al. 2020) and

2

may be brought to the surface as xenoliths in active volcanic arcs (Debari et al. 1987; Arai and Ishimaru 2008). Therefore, magmatic differentiation by lower crustal fractional crystallization of hydrous basalts is considered an important process in the formation of granodiorites and granites characteristic of the upper crust (Greene et al. 2006; Otamendi et al. 2012; Jagoutz 2014; Walker et al. 2015; Guo et al. 2020). Experimental studies (Müntener et al. 2001; Sisson et al. 2005; Nandedkar et al. 2014; Müntener and Ulmer 2018; Ulmer et al. 2018) and thermodynamic modeling (Annen et al. 2006; Jagoutz and Klein 2018) also support the hypothesis that deep (>0.7 GPa) differentiation of hydrous basalts can produce high-silica melts.

However, detailed experimental high-pressure crystallization studies suggest that differentiation in the deep crust cannot be solely responsible for the compositional stratification observed in arcs. Crystallization of hydrous primitive basalts in the lower crust (i.e. >0.7 GPa) produces peraluminous andesites, which are rarely observed in arc batholiths (Cawthorn and Brown 1976; Cawthorn and O'Hara 1976; Blatter et al. 2013; Nandedkar et al. 2014; Melekhova et al. 2015; Müntener and Ulmer 2018; Ulmer et al. 2018). Though the experimental basalts used in some of these studies are Al-enriched, their starting compositions are within the range of observed primitive arc basalts, as compiled by Schmidt and Jagoutz (2017). At lower crustal pressures and high (≥2 wt.%) water contents,

3

suppression of plagioclase and abundant early clinopyroxene crystallization drives residual melts towards peraluminous compositions (i.e., ASI > 1.1 where ASI = molar Al/(Ca-1.67×P+Na+K). In contrast, at lower pressures (<0.7 GPa) and/or lower water contents plagioclase and orthopyroxene (in the case of lower water activities) will saturate in a basalt at higher temperatures, limiting the increases in ASI in a crystallizing melt. As supported by high-pressure experimental studies, differentiation in arcs is not a simple story of high-pressure differentiation.

Thus, there are two observations that must be reconciled: (1) lower crustal arc sections dominated by ultramafic to mafic cumulates indicating the importance of deep crustal fractional crystallization and (2) experimental crystallization studies suggesting that although high-silica melts can be produced at these pressures, they will become peraluminous at relatively low SiO_2 contents (<60 wt.%), a feature rarely observed in arc batholiths. Three processes have been proposed to explain this apparent contradiction: (1) polybaric differentiation (Hamada et al. 2014; Melekhova et al. 2015), (2) mixing between low-Mg basaltic and granitic melts (Sisson et al. 1996; Grove et al. 2003; Sisson et al. 2005; Blatter et al. 2013; Müntener and Ulmer 2018), or (3) mixing of dry and wet magmas to produce "damp" (<2 wt.% H_2O) basalts to andesites that then further differentiate in the lower crust (Rezeau et al. 2021) (e.g., Sisson et al. 2005; Müntener and Ulmer 2018). All three of these processes require the presence of evolved (low-MgO)

4

basalts produced through lower crustal differentiation of more primitive, high-MgO basalts. However, each is not without its shortcomings. In scenario (1), the low-MgO basalts can ascend into the upper crust to differentiate further, producing non-peraluminous silicic melts. The absence of significant volumetrically significant mafic plutons in the upper crust of exposed arcs, however, suggests that this may be relatively minor process. In scenario (2), the low-MgO basalts mix with higher-silica melts (formed through fractional crystallization, partial melting, or both) to produce granodioritic magmas. However, mixing of two magmas with strongly contrasting viscosities is mechanically unviable (Sparks and Marshall 1986). Last, in scenario (3), the low-MgO basalts with variable water contents mix to produce a damp (<2 wt.% H_2O) basalt that then differentiates in the lower crust without significant alumina enrichment due to early orthopyroxene and plagioclase crystallization. However, although crystallization of damp basalts in the lower crust can ameliorate issues with ASI increases during differentiation, this model cannot explain other features of arc batholiths. For example, dry to damp differentiation of basalts will follow a tholeiitic trend (increasing FeO/MgO with SiO_2) which is not observed in the calc-alkaline batholiths of continental arcs (e.g. Villiger et al. 2004; Melekhova et al. 2015; Müntener and Ulmer 2018).

To test whether these processes play an important role in the generation of arc batholiths, this study focuses on an upper crustal mafic complex in a

continental arc batholith. Although less common than voluminous silicic plutons, upper crustal mafic intrusions potentially preserve information on the nature and origin of low-MgO basalts in the formation of arc batholiths. Here, we undertake a case study of the Hidden Lakes mafic complex (HLMC), an exposure of norite through monzonite emplaced into the upper crust of the Sierra Nevada batholith. We present detailed field mapping to document intrusive relationships and the range of mafic lithologies, and U-Pb zircon geochronology to determine the timing of crystallization of the HLMC relative to surrounding high-silica intrusions. Using bulk-rock and mineral chemistry data, as well as comparisons to experimental studies, we aim to constrain crystallization pressures, temperatures, H_2O content, and oxygen fugacity (fO_2) of the crystallizing magma. As field, petrographic, and geochemical data suggest a fractional crystallization origin for the HLMC, we construct a two-stage polybaric fractionational crystallization model to replicate the composition of the evolving melt. In light of our findings, we discuss the importance of evolved basalts in the formation of high-silica arc batholiths.

Geologic Setting

The HLMC is located in the eastern central Sierra Nevada batholith (SNB), the largely granodioritic intrusive product of the Sierra Nevada paleo-continental arc. From the late-Triassic through late-Cretaceous, magmatism related to

6

129 subduction of the Farallon plate beneath North America produced felsic intrusions
130 that now form the bulk of the batholith. Magmatism ceased by 75 Ma due to
131 shallowing of the subduction angle (English et al. 2003; Kirsch et al 2016).
132 Presently, most of the SNB is exposed to upper crustal depths (0.2 to 0.4 GPa),
133 with the exception of the southernmost lower crustal section which extends to 1.0
134 GPa pressures (Ague and Brimhall 1988; Pickett and Saleeby 1993). The late-
135 Jurassic (145-160 Ma) and late-Cretaceous (85-100 Ma) periods in the SNB are
136 characterized by enhanced magmatic activity, during which of 85% of the batholith
137 volume was generated (DeCelles et al. 2009; Ducea et al. 2015; Kirsch et al. 2016).
138 Numerous mafic bodies throughout the SNB upper crust were noted during
139 early studies of the batholith (Mayo 1941; Bateman and Eaton 1967; Frost 1987),
140 but have been less comprehensively studied as compared to the felsic batholith due
141 to their relatively small areal fraction of the exposed SNB. Geochronological
142 studies on a few of the mafic bodies demonstrate that they are coeval with the
143 surrounding granitoids and therefore may play a critical role in the formation of the
144 granitoid batholith (Coleman et al. 1995; Ratajeski et al. 2001). Several mafic
145 bodies have been investigated in previous studies (Frost 1987; Frost and Mahood
146 1987; Coleman et al. 1995; Sisson et al. 1996; Ratajeski et al. 2001; McCarthy and
147 Müntener 2016), all of which document the presence of hydrous, low-Mg basalts
148 in the upper crust of the SNB.

Field Relationships

The Hidden Lakes mafic complex (HLMC) is exposed in the central SNB near Bishop, CA, and covers an area of 2.5 km^2. Our field mapping (Fig 1) refines the outer margins of the mafic complex where it is in contact with surrounding granodiorite plutons, as previously mapped by Bateman (1992), and displays the variation in rock types and the nature of contacts within the mafic complex. Amphibole- and biotite-bearing medium- to fine-grained gabbros are the dominant lithology throughout HLMC. Norites occur as small pods within the gabbro in the eastern section of HLMC. In the northeastern section of HLMC, near its contact with the Round Valley Peak granodiorite, lithologies transition gradationally from gabbro to monzodiorite to monzonite toward the northern edge of the mafic complex. The field occurrences and characteristics of each rock type in the mapped area are described in detail below.

Norites

Norites are the most primitive lithology found in HLMC and are present as small, rounded pods (up to 3 m) within the gabbro unit in the eastern section of the complex (Fig S2a). Their volumetric abundance within the gabbro is difficult to ascertain due to exposure on steep cliff faces, however, they weather out and occur

8

as large boulders in the scree fields to the west of the cliffs. Norite boulders are significantly less abundant in scree fields than gabbro boulders, so it is presumed that norite is less common than gabbro in the cliff exposures.

Anorthosites

Anorthosite was observed only in rare boulders below gabbro-dominated cliffs in the southeastern section of HLMC (Fig 1). The anorthosite is medium-fine grained (0.5-2 mm), isotropic, and contains 90 to 95% dark grey plagioclase with 5 to 10% biotite.

Gabbros

Amphibole-biotite gabbro is the volumetrically dominant rock type in HLMC and is present in most areas of the mafic complex, except for the northern margin characterized by more evolved lithologies (Fig 1). The gabbros contain abundant plagioclase and amphibole, along with common clinopyroxene and biotite, and minor orthopyroxene. Based on their macroscopic textures, the gabbros are divided into three main groups: (1) medium-fine grained gabbro, (2) coarse-grained gabbro, and (3) "spotted" gabbro (Fig S2).

Medium-fine grained gabbro is the most common rock type in HLMC and contains dark gray plagioclase, amphibole, and pyroxene (1-3 mm) with evenly

9

distributed finer-grained biotite (~1 mm). The coarse-grained gabbro is present in elongate bodies within the medium-fine grained gabbro (Fig 1). The mineral assemblage in the coarse-grained gabbro is identical to the medium-fine grained gabbro, with slightly less plagioclase. The "spotted" gabbro is characterized by 1 to 2 cm clots of poikilitic amphibole+biotite enclosing pyroxene and minor plagioclase, which give it a spotted surface appearance (Fig S2). Clots are enclosed in a finer-grained matrix that is mineralogically very similar to the medium-fine grained gabbro.

Contacts between the different textural gabbroic units are gradational over 1 to 5 m, or can exhibit mingling textures. Elongate intrusion geometry is evident in the western and southern areas of HLMC, while the eastern section appears to be a single large intrusion composed mainly of medium-fine grained gabbro that grades into monzodiorite to the northeast.

Monzodiorites and Monzonites

In the northeastern section of HLMC, two bodies of monzodiorite and two elongate bodies of monzonite are in largely gradational contact with one another over >5 m. Mingling textures between the monzonite and monzodiorite, as well as dikes of monzonite intruding into monzodiorite, and vice versa, are present. Thus,

10

these are synmagmatic lithologies that were mobilized shortly after crystallization of the northeastern section of gabbro.

The monzodiorites are medium-fine grained, dominated by plagioclase, and contain biotite, K-feldspar, amphibole, and interstitial quartz in order of decreasing abundance. Rare clinopyroxene is present in the cores of amphibole grains. The monzonites are typically medium to coarse grained, dominated by plagioclase and clusters of biotite + amphibole. K-feldspar is more common than in the monzodiorites, and quartz is typically minor and interstitial.

Diabase Bodies

Generally small, irregularly shaped bodies of diabase, as well as diabase dikes, are present within and near HLMC. Intrusions are fine grained and occasionally contain blocks of HLMC gabbro. Contacts between the diabase and the mafic complex are sharp, in contrast with the generally gradational contacts between the coarser-grained lithologies, suggesting that the diabase is significantly younger than much of HLMC.

Surrounding Felsic Plutons and Outer Contacts

Three felsic intrusions are in contact with the HLMC around its perimeter: the granite of Chickenfoot Lake to the west and south, the Lake Edison

11

granodiorite to the east, and the Round Valley Peak granodiorite (Krv) to the north (Fig 1).

The granite of Chickenfoot Lake (Jcf, 191.6 ± 1.0 Ma, this study) is one of few Jurassic-aged plutons in the central SNB. Where observed, the contact between Jcf and HLMC is a 0.1 to 1 m wide gradational zone of dioritic composition that occasionally includes coarse orthoclase xenocrysts, which are not present in the adjacent gabbros and so presumably originated as crystals in Jcf (Fig S3b). Diorite dikes originating from HLMC inrtude into the Jcf. The Lake Edison granodiorite (Kle, 90.9 ± 0.1 Ma; Lackey et al. 2008) intrudes HLMC on its eastern side, creating a subvertical and sharp contact with Kle truncating layering in HLMC. The Round Valley Peak granodiorite (Krv) intruded at 88.8 ± 0.02 Ma (Lackey et al. 2008) and forms a complicated contact zone (the Heterogeneous Intrusive Zone) where it intrudes the northeastern margin of HLMC.

Heterogeneous Intrusive Zone

The east-west trending contact between Krv and HLMC is a ~150 m wide contact zone, which we term the Heterogeneous Intrusive Zone (HIZ). This zone consists of a magmatic breccia composed of 50 to 85% Krv granodiorite that has entrained angular to subangular blocks of gabbro, monzodiorite, and monzonite. Mafic blocks vary in size (5 cm-10 m) and angularity with the most angular blocks

present on the southern margin of HIZ. Blocks become progressively more rounded and partially digested towards the north (Fig S3c). Meter to sub-meter scale dikes of the Krv intrude the HLMC immediately south of the HIZ, and sometimes contain angular xenoliths of gabbro, monzodiorite, and monzonite from the HLMC (Fig S3d).

Petrography

Descriptions of 28 representative samples in thin section are given below, with at least three sections from each rock type. Modal percent of major minerals were estimated visually (Table 1).

Norites

The norites consist of orthopyroxene (15-75%), plagioclase (15-40%), amphibole (0- 20%), biotite (5-15%), clinopyroxene (1-5%) and olivine (<1%), along with minor Fe-Ti oxides and accessory apatite and zircon. Norite samples exhibit ad- and mesocumulate textures with rounded orthopyroxene grains that range in size from 50 to 600 μm (Fig 2a). All samples contain interstitial plagioclase and few contain euhedral plagioclase crystals ranging from 0.2 to 3 mm. Amphibole occurs either as large oikocrysts (1 cm) enveloping orthopyroxene and plagioclase ± olivine (Fig 2b), or as overgrowths on orthopyroxenes and

13

clinopyroxenes (Fig S4a). Late crystallizing biotite (0.4-2 mm) fills interstitial spaces and surrounds rounded orthopyroxenes. Olivine was observed in two samples (0.2-1 mm). Minor Fe- and Fe-Ti-oxides are included in orthopyroxene and plagioclase.

Gabbros

The relative proportions of mineral phases in the gabbros are variable, with the following ranges: plagioclase 45 to 75%, amphibole 5 to 50%, clinopyroxene 5 to 20%, biotite 5 to 10%, and orthopyroxene 0 to 5%. Gabbros with both cumulative and non-cumulative textures are present in HLMC (Fig 2c,d). Coarse-grained and spotted gabbro samples, as well as some of the medium-fine grained gabbros, preserve textural evidence for accumulation of plagioclase and clinopyroxene. These meso- to adcumulate samples are dominated by equant, nearly euhedral plagioclase (0.5-4 mm) and rounded clinopyroxene (0.5-3 mm) crystals. Orthopyroxene is far less prevalent than clinopyroxene, and both pyroxenes commonly contain exsolution lamellae. Amphibole is present as a primary magmatic phase, secondary magmatic rims nucleated on pyroxenes, and as psuedomorphs after pyroxene (Fig 2c, Fig S4b). Biotite is a late crystallizing interstitial phase containing inclusions of clinopyroxene, plagioclase, and Fe-Ti-oxides. Small, rare alkali feldspars are present interstitially.

14

288

289 *Monzodiorites and Monzonites*

290 The monzodiorites and monzonites of HLMC are distinguished from the
291 gabbros by a decreased abundance of pyroxene, though many monzodiorites
292 contain pseudomorphs of pyroxene altered to amphibole. These pseudomorphs
293 occasionally have ortho- and clinopyroxene cores. The monzodiorites consist of 60
294 to 70% plagioclase, 15 to 20% biotite, 10 to 15% K-feldspar, 5 to 15% amphibole,
295 <2% quartz, and minor ortho- and clinopyroxene (0- 2%). All three occurrences of
296 amphibole are common (primary magmatic, secondary magmatic, and
297 pseudomorphic). Amphibole, biotite, and Fe-Ti-oxides are often found together in
298 1-3 mm clots (Fig S4c).

299 The monzonites contain 40 to 60% plagioclase, 20 to 35% K-feldspar, 10 to
300 20% biotite, 0 to 5% amphibole, and minor quartz (<5%). Euhedral to subhedral
301 primary magmatic amphibole grains (0.3-1.5 mm) lie between generally coarse
302 anhedral plagioclase and K-feldspars. Irregularly shaped flakes of biotite (0.5- 2
303 mm) are packed between plagioclase crystals and can be included in K-feldspars
304 (Fig S4d). Quartz (up to 0.5 mm) occurs interstitially.

305

RESULTS

Zircon U-Pb isotopic measurements, bulk-rock major and trace element concentrations, and mineral chemistry data are included along with sample GPS locations in the Supplementary Data File (Tables S1-S3). Analytical methods are described in the Supplementary Material.

Geochronology

Zircon from six total samples of monzodiorite and monzonite from the HLMC were dated using laser ablation inductively coupled mass spectrometry (LA-ICPMS) at the University of California, Santa Barbara, and one granite sample was dated using LA-ICPMS at the Arizona Laserchron Center. All dated HLMC samples (not including the granite sample) are late Cretaceous in age. Weighted mean crystallization ages and 2σ errors for monzondiorite samples are 95.1 ± 1.0 Ma for SNB-16-6, 95.6 ± 0.8 Ma for SNB-16-9, and 96.5 ± 0.8 Ma for SNB-14-34. HL-17-2, an anorthosite, has an age of 95.7 ± 0.7 Ma. The monzonite ages are 96.3 ± 0.8 Ma for SNB-16-12 and 90.5 ± 0.8 Ma for SNB-14-40. These ages allow for up to 6 Ma of magmatic activity in HLMC and constrain crystallization ages of the more mafic parts of the HLMC at 5 and 7 million years older than the Lake Edison granodiorite (90.9 ± 0.1 Ma; Lackey et al. 2008) and Round Valley Peak granodiorite (88.8 ± 0.02 Ma; Lackey et al. 2008),

16

respectively. HLMC is significantly younger than the granite of Chickenfoot Lake (at 191.6 ± 1.0 Ma, this study). These ages are consistent with field relationships, in which HLMC lithologies are observed intruding into Jcf and intruded by Kle and Krv. Sample SNB-14-40, a monzonite from the northern edge of the mafic complex near the contact with Krv, has a crystallization age ~5 Ma younger than the other five mafic samples (90.5 ± 0.8 Ma). This may represent a late stage melt associated with differentiation of HLMC magmas that was remobilized by intrusion of Kle, as their ages overlap within uncertainty. We presume that the gabbros and norites crystallized within the range of monzodiorte ages (95.1-96.5 Ma), though neither of these more mafic lithologies were directly dated due to the rarity of zircon.

Bulk-rock Major Element Chemistry

Major element bulk compositions from HLMC were analyzed via X-ray fluorescence (XRF) spectrometry at Caltech, following methods in Bucholz and Spencer (2019). Samples display a trend of magmatic evolution that straddles the boundary between a monzonitic series and granodioritic series (Bas et al. 1986; Middlemost 1994). For simplicity, we retain the lithology names norite, gabbro, monzodiorite and monzonite as classified based on mineralogy in previous sections, even if all samples of one lithology do not fit precisely within a single

17

chemically defined field (Fig 3a). SiO_2 contents from the full suite of HLMC samples range from 43.6 to 62.0 weight percent (wt.%) and molar Mg numbers (Mg# = 100×Mg/[Mg+Fe])calculated using total Fe) range from 73 to 46 (Fig 3d). Aluminum saturation index (ASI) values of HLMC samples range from 0.57 to 0.96 (ASI= Al/ [Ca-1.67×P+ Na+ K]), indicating that all sampled lithologies are metaluminous.

The norites represent the most primitive cumulates to crystallize from an HLMC melt, based on their high Mg#s (73.1-64.6). The norites contain 49.8 to 53.6% SiO_2, 10.2 to 20.0 wt.% MgO, and 9.8 to 14.8 wt.% FeO. Relatively constant SiO_2 content with decreasing MgO and FeO reflects increasing abundance of plagioclase relative to orthopyroxene with progressive fractionation. Likewise, co-variation in CaO (3.0-7.7 wt.%, Fig 3c) and Al_2O_3 (4.9-12.9 wt.%) is controlled by the proportion of plagioclase relative to clinopyroxene, orthopyroxene, and olivine. To highlight the differences in mineral abundances, we separate the norites into two groups: high-Ca norites (CaO≥7.5 wt.%) and low-Ca norites (CaO < 6 wt.%), with a compositional gap from 6 to 7.5 wt.% CaO (Figure 3b). In general, the more differentiated norite samples (high-Ca group) have slightly lower SiO_2 contents, significantly lower MgO and FeO contents, and elevated TiO_2, CaO, Al_2O_3, K_2O, Na_2O as compared to the low-Ca group. ASI varies from 0.57 to 0.72 in the norites but does not clearly correlate with SiO_2.

18

366 The sequence of gabbros through monzonites follows a trend of increasing
367 SiO_2, K_2O, and Na_2O contents with decreasing MgO, FeO, CaO, Al_2O_3, and TiO_2
368 contents (Fig 3 and S10). ASI gradually increases from 0.70 to 0.96 from the
369 gabbros to the monzonites, in accordance with a decrease in the modal abundance
370 of calcic amphiboles relative to Al-bearing phases. Gabbros are the most
371 voluminous rock type in HLMC and fall into two groups based on major-element
372 concentrations: 1) low-SiO_2 gabbros, with 43.9 to 46.8 wt.% SiO_2 and 2) high-SiO_2
373 gabbros, with 49.2 to 52.5 wt.% SiO_2. The low-Si gabbros have higher proportions
374 of Fe-Ti oxides and pseudomorphic amphiboles relative to clinopyroxenes in the
375 high-SiO_2 gabbros, while high-SiO_2 gabbros contain a greater modal abundance of
376 plagioclase. Al_2O_3 contents are significantly higher in the gabbros (17.3-23.4
377 wt.%) than the norites due to greater abundance of plagioclase and lower
378 abundance of orthopyroxene. The highest Al_2O_3 concentration (23.4 wt.%) is at
379 52.2 wt.% SiO_2, then gradually decreases with increasing silica content through the
380 monzodiorites and monzonites.

381 Two samples from cross-cutting diabase dikes and pods are shown to have
382 very different Mg#s (64.1 and 42.6) despite similar SiO_2 content (47.0 and 49.2
383 wt.%). The lower Mg# sample has considerably higher alkali (Fig 3a) and P_2O_5
384 (0.84 wt.%) concentrations than other HLMC samples with similar silica contents
385 (~0.25-0.4 wt.%), so this sample is unlikely to be co-genetic with HLMC. The

19

386 higher Mg# diabase is similar in composition to the least primitive norites or
387 highest Mg# gabbros, and therefore may be related to the HLMC system.
388
389 **Bulk-rock Trace Element Chemistry**
390 Trace element concentrations were collected with solution ICPMS, using
391 acid-digested chips of the glass disks used in XRF analyses. All norite samples
392 have low Sr concentrations (89-407 ppm) that increase with increasing modal
393 abundance of plagioclase (Fig 3e). Higher Sr contents (705-1030 ppm) in the
394 gabbros are reflective of higher plagioclase abundance. Sr contents in the
395 monzodiorites (659-921 ppm) and monzonites (604-934 ppm) overlap with and
396 extend to slightly lower values compared to the gabbros. Sr/Nd and Al/Si ratios,
397 and Eu anomalies are positively correlated and indicate the extent of plagioclase
398 accumulation. Primitive mantle normalized Eu anomalies ($Eu/Eu^* = Eu_N / sqrt[Sm_N$
399 $\times Gd_N]$) are < 1 in the norites (0.45-0.78) and 0.72 to 1.46 in all other HLMC
400 lithologies.
401 The norites have relatively high Ni and Cr contents (97-504 ppm and 123-
402 551 ppm, respectively, Fig 3f and S11), which reflect the abundance of
403 orthopyroxene (up to 75%) in these samples, as well as the presence of minor
404 olivine and clinopyroxene. Ni and Cr contents are low in the low-SiO_2 gabbro

group (3-24 ppm Ni, 2-21 ppm Cr), then increase slightly, on average, in the high-SiO_2 gabbros and remain relatively constant in the monzodiorites and monzonites.

On primitive-mantle normalized spider diagrams (Fig 4), all samples display strong Nb and Ta depletions and Pb enrichment consistent with a subduction-related origin for the HLMC parental melts (Miller et al. 1994; Stolz et al. 1996). Most of the gabbros, particularly the low-SiO_2 gabbros, exhibit Ti enrichments as controlled by crystallization of Fe-Ti-oxides, biotite, and titanite. Significant titanium depletions are observed in the norites, as these samples lack titanite. Besides the norites, all lithologies display Sr enrichment, reflecting accumulation of plagioclase in higher abundances than olivine and pyroxenes. Some norites are considerably enriched in LIL elements, particularly Cs and Rb (up to 34 and 50 ppm, respectively), likely due to biotite crystallization. In the more evolved rocks and in two norites (Fig 4a, b, f-i), relative enrichments in Zr and Hf are observed due to the presence of zircon.

Rare earth elements (REEs) and other incompatible element concentrations (Ba, Th, Nb, Pb, Hf, Ta, U, Rb, Zr) are positively correlated with SiO_2. HREE elements are depleted relative to LREE elements in all rock types, and La/Yb ratios increase with increasing silica content, though there is significant overlap between rock types.

21

Classification of Cumulate and Liquid-Like Samples

Based on textural and compositional parameters, we classify each sample as having a liquid-like or cumulate bulk composition. All norites are classified as cumulates because cumulate textures were identified in all norite thin sections (Fig 2a), and their bulk-rock Mg#s are significantly higher than the rest of the HLMC (Mg#= 64.6-73.1, with a gap in HLMC from 57.8-64.6). Gabbro textures are variable from meso- or orthocumulates, to randomly oriented masses of interlocking crystals (Fig 2d). The latter is suggestive of rapidly crystallized melt-like lithologies. In addition, we use Al/Si and Sr/Nd ratios as tracers of plagioclase accumulation (Jagoutz 2010; Bucholz et al. 2014) and define cumulate gabbros as those with Al/Si > 0.21 and cumulate monzodiorites and monzonites as those with Sr/Nd > 30 (Fig 5a). These values place samples with textural observations into the correct categories and allows us to classify samples for which we do not have petrographic constraints.

When compared to the macroscopic rock textures, all liquid-like gabbros are medium-fine grained gabbros, and all coarse-grained and spotted gabbros are cumulates. Some medium-fine grained gabbros are also classified as cumulates based on our compositional criteria. Eu anomalies are variable within rock types, and either similar between liquids and cumulates of the same rock type (e.g., liquid-like monzodiorites and cumulate monzodiorites), or slightly elevated in the

22

445 cumulate group. Eu anomalies are <1 in the norites (0.45-0.69), reflecting minimal
446 plagioclase accumulation and incompatibility of Eu^{2+} in olivine and orthopyroxene
447 (Fig 5b).
448
449 **Mineral Chemistry**
450 Major element compositions of minerals were completed using electron
451 probe microanalysis (EPMA) on roughly 3 to 10 grains per phase in each sample.
452 In zoned crystals, at least 3 points were analyzed in each grain to assess core-to-
453 rim compositional variation. Selected mineral compositions are summarized in Fig
454 6, and additional variation diagrams and geochemical data are included in the
455 Supplementary Files (Fig S5-S8, Table S3).
456
457 *Olivine*
458 Olivine is rare in HLMC and present only in two low-Ca norite samples,
459 SNB-14-62 and SNB-14-52. The highest Mg# olivine analyses are found as
460 chadacrysts within in large amphibole oikocrysts. Olivine chadycrysts have Mg#s
461 ranging from 80 to 81, while non-chadacrystic olivine grains have Mg#s ranging
462 from 79 to 80, while olivines from cumulate xenoliths crystallized in the SNB
463 lower crust extend to Mg# 92 (Dodge et al. 1986; Lee et al. 2001). Olivines have
464 0.28 to 0.35 wt.% MnO, which is negatively correlated with Mg# (Fig 6a).

Orthopyroxene

Orthopyroxene is abundant in the norites, occasionally present in the gabbros, and rare in the monzodiorites and monzonites where it is found only in amphibole cores. The Mg# of orthopyroxenes decreases from the norites (65-80) to the gabbros (51-65). In the monzodiorites and monzonites, compositions significantly overlap with those in the gabbros (Mg# = 49-59), suggesting that these lithologies experience an early interval of orthopyroxene crystallization followed by amphibole crystallization.

Orthopyroxene Cr_2O_3 contents generally decrease with decreasing Mg# and vary from 0.01 to 0.11 wt.% in the norites and are below detection limit to 0.03 wt.% in the gabbros, monzodiorites, and monzonites. Similarly, Al_2O_3 is positively correlated with Mg#, ranging from 0.35 to 2.1 wt.% in the norites and 0.29 to 1.1 wt.% in all other orthopyroxene-bearing lithologies (Fig 6b). MnO increases with decreasing Mg# and varies between 0.30 and 0.55 wt.% in the norites, and 0.59 and 1.1 wt.% in the gabbros and monzodiorites. The monzonites have slightly higher orthopyroxene MnO concentrations of 0.95 to 1.2 wt.%.

There is a significant range in orthopyroxene Al_2O_3 contents in the SNB xenoliths (0.7-5.4 wt.%; Dodge et al. 1986; Lee et al. 2001), likely due to crystallization at a range of temperatures and pressures. Mg#s of these grains

24

485 overlap with compositions in the norites and gabbros, as well as extend to higher
486 Mg#s (maximum 92).
487
488 *Clinopyroxene*
489 Clinopyroxene is a minor phase in the norites (<5% modal abundance),
490 common in the gabbros, and occasionally present in the cores of amphiboles in the
491 monzodiorites and monzonites. In the norites, clinopyroxene Mg#s range from 73
492 to 79 and decrease from individual grain cores to rims. Analogous to the
493 orthopyroxenes, clinopyroxene compositions in the gabbros, monzondiorites, and
494 monzonites are very similar to one another. In particular, the clinopyroxenes from
495 the cumulate gabbros and the liquid-like monzondiorites overlap significantly in
496 Mg#, which may indicate that these clinopyroxenes in HLMC may have
497 crystallized from a melt similar to the gabbros. Clinopyroxene Mg#s vary from 61
498 to 73 in the gabbros, 61 to 75 in the monzodiorites, and 60 to 68 in the monzonites.
499 Clinopyroxene Cr_2O_3 contents are roughly correlated with Mg#, ranging
500 from 0.03 to 0.11 wt.% in the low-Ca norites, 0.02 to 0.03 wt.% in the high-Ca
501 norites, and commonly below detection limit (~0.015 wt. %) in all other rock
502 types, with a maximum of 0.04 wt.%. Clinopyroxene MnO content increases
503 consistently with decreasing Mg# (from 0.18 to 0.56 wt. %). Al_2O_3 content is
504 variable between 0.47 and 2.8 wt.%, commonly decreasing (~75% of grains) and

505 occasionally increasing (~25% of grains) from crystal cores to rims. Al_2O_3 in
506 clinopyroxene cores increases from the norites (0.56-1.28 wt.%) and peaks at 1.79
507 wt.% in the liquid-like gabbros, then decreases through the gabbros,
508 monzodiorites, and monzonites to 1.09 wt.%. This peak corresponds to the
509 maximum in bulk-rock Al_2O_3 concentration.
510
511 *Amphibole*
512 Amphibole is present in all rock types in HLMC and may be a primary
513 magmatic phase, secondary magmatic overgrowth on pyroxene crystals, or
514 pseudomorphic replacement of pyroxene due to reaction with an evolving melt.
515 There is no distinct compositional difference between these occurrences, however
516 pseudomorphic amphiboles contain abundant plagioclase micro-inclusions.
517 Amphibole compositions are dominated by magnesiohornblende based on the
518 classification of Leake et al. (1997). Analyses with <0.75 formula units of Al
519 (calculated on a 23-oxygen basis) are considered metamorphic alteration products
520 and not further discussed. Nearly all amphibole in the high-SiO_2 gabbros (cumulate
521 and liquid-like) is actinolite, while all other rock types contain magmatic
522 amphibole.
523 There are two compositional populations of amphiboles in the low-Ca
524 norites, which are distinguishable by their aluminum contents and both fall under

26

525 the classification of magnesiohornblende (Fig 6c). Mg#s of both groups are
526 comparable, with the high-Al population ranging from 71 to 77 and the lower-Al
527 population ranging from 72 to 79. The high-Al population (9.6-12.8 wt.% Al_2O_3) is
528 characterized by primary magmatic oikocrysts that surround olivine grains and is
529 only present in samples SNB-14-52 and SNB-14-62 (*c.f.*, Fig 2b). This population
530 is also high in TiO_2 (2.9-3.6 wt.%) and Na_2O (1.7-2.3 wt.%) compared to other
531 amphiboles in the norites with similar Mg#s (0.2-1.3 wt.% TiO_2 and 0.6-1.1 wt.%
532 Na_2O). The lower-Al population (4.5-5.9 wt.% Al_2O_3,) appears to also be of
533 primary magmatic origin based on the euhedral to subhedral crystal shapes. These
534 two populations are not observed in the same samples and so may indicate slight
535 compositional variation between different norite pods. All amphiboles in the high-
536 Ca norites are similar in composition with Mg#s ranging from 67 to 71 and Al_2O_3
537 varying between 4.8 and 6.3 wt.%. Amphibole Mg#s in the gabbros and
538 monzodiorites are negatively correlated with Al_2O_3 in a series of parallel trends,
539 which each represent within-sample compositional variation reflecting sub-solidus
540 Tschermak exchange, a trend that is not evident in amphiboles from the norites.
541 Similarly, TiO_2 and Na_2O are negatively correlated with Mg# within individual
542 samples. Amphibole MnO content increases with decreasing Mg# and is relatively
543 constant within each rock type, ranging from 0.09 to 0.31 wt.% in the norites, 0.21
544 to 0.34 wt.% in the gabbros, 0.28 to 0.59 wt.% in the monzodiorites, and 0.48 to

0.62 wt.% in the monzonites. CaO content is negatively correlated with Mg#, though there is considerable overlap between rock types.

Biotite

Biotite is present in all rock types, typically interstitially, and is thus interpreted as a late crystallizing phase. The Mg# of biotite in the low-Ca norites ranges from 54 to 76, with a compositional gap between 59 and 63. The high-Mg# biotite group extends to higher TiO_2 (2.4-5.2 wt.%) and F (0.42-0.81 wt.%) than the low-Mg# group (1.7-4.1 and 0.32-0.43 wt.%, respectively). There is no clear textural difference between the low- and high-Mg# biotite, though individual samples only contain biotite from one compositional group. Biotite Mg# decreases to the high-Ca norites (52-60) and gabbros (47-61). The range of biotite Mg#s in the monzondiorites (45-58) overlaps with that of the gabbros and the monzonites (47-52).

MnO contents systematically increase with decreasing Mg#, from 0.02 to 0.18 wt.% in the norites to a maximum of 0.43 wt.% in the monzonites. Al_2O_3 content of biotite in the norites is variable (11.9-14 wt.%) and not clearly correlated with Mg#. There is significant overlap in Al_2O_3 contents in biotite for the remainder of the studied lithologies (13.2-15.8 wt.% in gabbros, 12.9-16.3 wt.% in monzondiorites, 12.5-15.6 wt.% monzonite). Within individual samples,

28

565 there is a weak positive correlation between Mg# and Al_2O_3 content of biotite,
566 which is the opposite correlation from what is predicted by Tschermak exchange,
567 and suggests minimal subsolidus alteration. Na_2O contents reach 0.18 wt.% in
568 high-Mg# biotite in the norites, and is <0.11 wt.% in other lithologies, and often
569 below detection limit. Fluorine decreases with decreasing Mg#, following
570 established Fe-F avoidance trends (Fig 6d) (Mason 1992; Icenhower and London
571 1997). Biotite F content ranges from 0.32 to 0.91 wt.% in the norites, and in other
572 rock types biotite contains between 0.19 and 0.54 wt.% F.
573
574 *Feldspars*
575 Plagioclase feldspar is dominantly interstitial in the norites, though
576 occasional euhedral crystals are present, and is a common fractionating phase in all
577 other HLMC rock types. The anorthite content (An) of interstitial plagioclase in
578 norites is highly variable, ranging from An_{29} to An_{72}, while euhedral plagioclase
579 has approximately An_{82}. Euhedral to subhedral plagioclase in the gabbros can have
580 distinct core and rim compositions with An_{76} to An_{92} cores and An_{40} to An_{62} rims.
581 In crystals without a core-rim compositional difference, the composition is
582 comparable to the aforementioned rims. Distinct cores and rims are present in <5%
583 of plagioclase crystals in the monzodiorite plagioclase and absent from the

584 monzonites. Plagioclase is An_{27} to An_{58} in rims and ~An_{77} in cores in the
585 monzodiorites, and An_{31} to An_{54} in the monzonites.
586 Alkali feldspar is found as small, interstitial grains in the norites and
587 gabbros, but becomes increasingly common in the monzodiorites and monzonites.
588 Orthoclase (Or) and albite (Ab) content is similar for all rock types, with variation
589 between $Or_{72}Ab_{18}$ and $Or_{98}Ab_{2}$.
590
591 *Zircon*
592 Zircon grains from HLMC have Ti concentrations ranging from 2 to 24 ppm
593 in the monzonites, 4 to 31 ppm in the anorthosites, and 5 to 27 ppm in the
594 monzodiorites. Zircon is rare in the gabbros and norites and was therefore not
595 separated for analysis. Hf concentration is negatively correlated with Ti
596 concentration within each sample, ranging from 8610 to 17100 ppm, with 2470 to
597 7670 ppm of intra-sample variation.
598 REE concentrations of melts in equilibrium with the zircons were calculated
599 using the methods of Chapman et al. (2016) (Fig S9). Primitive mantle normalized
600 REE (plus Nb and Y) patterns of calculated melts are nearly parallel to the
601 corresponding whole-rock patterns. In cumulate samples, calculated melt
602 compositions are similar to the whole rock concentrations in the LREE, and
603 slightly higher or lower in the HREE. Calculated melts have Eu anomalies <1

604 (0.70-0.81) that are slightly lower or equal within error (2 sigma of all analyses
605 within a sample) than in the corresponding whole rock composition, implying that
606 zircon saturation occurred after some plagioclase fractionation.
607
608 **DISCUSSION**
609 **Crystallization Conditions**
610 Out best estimates for crystallization pressures, temperatures, H_2O content,
611 and fO_2 and of HLMC lithologies are summarized in Table 2 and described below.
612 *Pressure*
613 We perform Al-in-hornblende barometry calculations using amphibole
614 analyses from monzonites, as this is the only HLMC lithology that contains the
615 requisite phase assemblage for this calibration (Mutch et al. 2016). Additionally,
616 these samples exhibit a lesser degree of Tschermak exchange than the gabbros and
617 monzodiorites, a process which could result in inaccurately low calculated
618 pressures. Using high-Al (7.5-8.8 wt.% Al_2O_3), low-Mg# (46-56) amphibole
619 analyses (i.e., those inferred to have experienced the least Tschermak exchange)
620 we calculate pressures of 0.30 to 0.34 GPa. Assuming an average density of 2.8
621 g/cm^3 for the overlying largely granitic crust (Christensen and Mooney 1995), this
622 equates to an approximate depth between 11 and 13 km.
623

Temperature

We use a variety of mineral thermometers to constrain crystallization temperatures across the range of HLMC lithologies. For these calculations, we utilize analyses from the rims of adjacent grains to give the best estimate of equilibrium compositions. In the gabbros, orthopyroxene and clinopyroxene pairs are out of Fe-Mg equilibrium, with partition coefficients ($[Fe/Mg]_{cpx}/[Fe/Mg]_{opx}$) of 0.65-0.86 as opposed to the equilibrium value of 1.09 ± 0.14 (Putirka 2008). This is not surprising due to the presence of pervasive exsolution lamellae for samples with coexisting ortho- and clinopyroxene. Thus, two-pyroxene equilibrium temperatures of 760 to 950 °C (Köhler and Brey 1990; Putirka 2008) likely represent cooling, rather than primary crystallization temperatures. The norites, however, lack discernable pyroxene exsolution and contain little to no clinopyroxene that could react with the available orthopyroxene. Orthopyroxene in the norites has CaO contents ranging from 0.6 to 1.6 wt.%, yielding crystallization temperatures of 900 to 1170 °C based on the Ca-in-orthopyroxene thermometer of Köhler and Brey (1990).

Evidence of subsolidus chemical exchange is found in amphibole analyses in the gabbros, monzondioites, and monzonites, as intra-sample negative correlation between Mg# and Al_2O_3 in amphibole suggests alteration of the original magmatic compositions by Tschermak exchange (Fig 6c). However, in the norites, amphibole

32

644 is present in two distinct compositional populations that do not define a continuous
645 trend of decreasing Al_2O_3 with increasing Mg#, which we interpret as preserving
646 magmatic amphibole compositions. In the gabbro, monzonite, and monzodiorite
647 samples, we calculate crystallization temperatures based on amphibole
648 compositions with realtively high Al_2O_3 contents (>7.5 wt.%) to avoid sites
649 significantly affected by subsolidus alteration. We do not report crystallization
650 temperature estimates from the pseudomorphic amphibole grains, as these are
651 likely out of equilibrium due to incorporation of excess Ca from the reaction of
652 melt + clinopyroxene $\rightarrow$ melt + amphibole into the plagioclase needed for
653 temperature calculation.

654 Thermometry based on the SiO_2 and anorthite contents of coexisting
655 amphibole and plagioclase, respectively, (Blundy and Holland 1990) defines a
656 wide range of crystallization temperatures within HLMC depending on the rock
657 type. As analyses of amphiboles in the norites do not follow a trend of decreasing
658 Al_2O_3 content with increasing Mg# as expected if significant Tschermak exchange
659 has significantly affected the mineral compositions, we believe the estimated
660 temperatures from the norite samples are representative of crystallization
661 conditions. Calculated crystallization temperatures of amphibole oikocrysts and
662 associated plagioclase in the norites are 865 to 950 °C, using amphibole SiO_2
663 contents ranging from 40.5 to 42.9 wt. % and plagioclase compositions of An_{58} to

33

664 An_{61}. Estimates from non-oikocrystic amphibole in the same samples are
665 significantly lower, ranging from 700 to 765 °C, using amphibole SiO_2 contents
666 ranging from 46.5 to 50.5 wt. % and plagioclase compositions between An_{23} and
667 An_{52}. Locally elevated H_2O contents in some norite pods may have allowed for
668 earlier amphibole saturation in some norites, as the oikocrystic, high-Al
669 amphiboles are not found in all norite samples. The high-Al oikocrysts likely
670 crystallized earlier in the fractionation sequence than the low-Al amphiboles, as
671 they record higher crystallization temperatures and contain inclusions of olivine,
672 which are not found in the low-Al amphiboles. The lack of olivine inclusions in the
673 low-Al amphiboles may indicate that olivine was lost from the fractionating
674 assemblage in favor of orthopyroxene prior to crystallization of the low-Al
675 amphiboles.

676 In the gabbros, primary and secondary (i.e., rims on pyroxenes) magmatic
677 amphibole temperatures are indistinguishable from one another and range from
678 740 to 880 °C (SiO_2 in amphibole 44.3-50.6 wt.%, anorthite content An_{37-81}). Using
679 the same method, monzodiorites and monzonites yield amphibole-plagioclse
680 crystallization temperatures of 815 to 870 °C (SiO_2 in amphibole 42.6-48.6 wt.%,
681 anorthite content An_{35-52}), and 800 to 850 °C (SiO_2 in amphibole 41.8-45.2 wt.%,
682 anorthite content An_{34-51}), respectively.
683

Water Content and Oxygen Fugacity

Relatively early crystallization of amphibole, and to a lesser extent biotite, in the HLMC fractionation sequence requires a hydrous parental melt. We apply the plagioclase-liquid hygrometer of Waters and Lange (2015) to plagioclase cores in the liquid-like gabbros to estimate melt H_2O content. Plagioclase core compositions are used because they represent the earliest crystalized sections, which are most likely to be in equilibrium with the bulk-rock "melt" composition. Using 990 to 1100°C as the temperature range for the onset of gabbro crystallization in HLMC based on experimental studies at upper crustal pressures and bulk compositions similar to the HLMC gabbros (Grove et al. 2003; Hamada and Fujii 2008), we estimate H_2O contents of 2.9 to 3.5 wt.% in the liquid like gabbros.

Oxygen fugacities (fO_2) play a significant role in the Fe-Mg partitioning into ferromagnesian minerals during crystallization. Oxygen fugacities elevated above that for mid-ocean ridge basalts (near the fayalite-magnetite-quartz buffer) are expected, as arc magmas are commonly characterized by fO_2 at NNO or higher (Sisson et al. 2005; Kelley and Cottrell 2009; Rowe et al. 2009; Brounce et al. 2014). Applying the oxybarometer of Loucks et al. (2020), which utilizes the concentrations of U, Ti, and Ce in zircon grains, we find a range of fO_2 values from ΔNNO -1.6 to 1.3 in the dated grains from monzodiorite and monzonite samples,

35

with an average fO_2 of ΔNNO -0.5. We use biotite and bulk-rock compositions and MELTS thermodynamic modeling to calculate fO_2 as presented in Bucholz et al. (2018) for melt-like monzonite SNB-16-9, which contains a relatively narrow range of biotite compositions (Fig 6d and S6) and thus subsolidus reequilibration was likely minimal. We find that the HLMC melts are oxidized to between NNO and ΔNNO +0.6 (± 1 log unit).

Comparison to Previous Studies

Our results from Al-in-hornblende barometry indicate a crystallization pressure of between 0.30 and 0.34 GPa, which is consistent with previous studies and show that the SNB around HLMC crystallized in the upper crust. The central SNB exposes dominantly upper crustal intrusions that crystallized between 0.1 to 0.4 GPa. Previous studies place the location of HLMC at pressures of 0.2 to 0.3 GPa (Ague and Brimhall 1988; Chapman et al. 2012), and 0.3 to 0.35 GPa (Nadin et al. 2008).

The following experimental studies were selected for comparison as they produce the series of mineral assemlages observed in HLMC. Our upper temperature estimate for the norites based on the Ca-in-orthopyroxene thermometer (1170 °C) is similar to experiments by Hamada and Fuji (2008), which produce an olivine + orthopyroxene + plagioclase assemblage from a high-

MgO basalt starting at 1160 °C, 0.4 GPa, 1.6-2.7 wt.% H_2O, and one log unit above the Ni-NiO buffer (ΔNNO+1). Clinopyroxene appears in the experimental assemblage at 1130 °C, and the assemblage of orthopyroxene + clinopyroxene + plagioclase + Fe-oxides continues to 1100°C and the termination of the experiment. The assemblage orthopyroxene + clinopyroxene + plagioclase + amphibole first crystallizes at 990 °C, 0.2 GPa, NNO, and 4.5 wt.% H_2O in experiments by Grove et al. (2003). Based on these two studies, which replicate the mineral assemblages found in the norite and gabbro cumulates in HLMC and bracket the pressure and H_2O content estimates for the HLMC and were performed at similar fO_2 conditions, the onset of gabbro fractionation, characterized by common clinopyroxene and minimal orthopyroxene, likely occurred between 1100 and 990 °C.

Experiments by Blatter et al. (2013) using an arc basalt starting material similar to HLMC melt-like gabbro compositions first crystallize amphibole + orthopyroxene + clinopyroxene + plagioclase from a primitive high-Al arc basalt at 0.4 GPa, 1000 °C, and 4 wt% H_2O. However, in these experiments orthopyroxene and clinopyroxene are present in roughly equal proportions and olivine is not present, unlike the HLMC norites. Orthopyroxene is part of the fractionating assemblage of mid-ocean ridge dacites during 0.2 GPa crystallization experiments under oxidizing conditions (NNO +1 to +2.1) with H_2O contents between 0.8 and 2

37

744 wt.% (Erdmann and Koepke 2016). At higher water contents (>2 wt.%) in these
745 experiments, the assemblage lacks orthopyroxene. The dominance of
746 orthopyroxene over clinopyroxene in the first crystallized HLMC cumulates
747 indicates a reduced H_2O content compared to Blatter et al. (2013), but the early
748 crystallization of amphibole suggests H_2O contents higher than in experiments
749 conducted by Erdmann and Koepke (2016) (H_2O > 2 wt.%). Experimental
750 evidence thus constrains the H_2O content of the HLMC parental melt between 2
751 and 4 wt.%.

752 In the HLMC norites, amphibole oikocrysts containing olivine imply that
753 these phases coexist in the magma. Crystallization experiments of Krawczynski et
754 al. (2012) limit the stability of the crystallizing assemblage of olivine + amphibole
755 to between an fO_2 of NNO and ΔNNO +3 at 0.3 GPa at the calculated
756 crystallization temperature of the oikocrystic amphiboles (~950 °C). This study
757 complements our fO_2 calcultions in the monzodiorites and monzonites (fO_2 ~NNO-
758 ΔNNO+0.6), and shows that the parental melt to HLMC was similarly oxidized in
759 comparison to the more evolved lithologies.

760

761 **A Cogenetic Fractionation Sequence**

762 *Field and Petrographic Evidence*

38

763 The western limb of HLMC is composed of mainly medium-fine grained
764 gabbro with elongate, N-S trending texturally distinct gabbro bodies (coarse-
765 grained and spotted gabbros, Fig 1). All coarse-grained and spotted gabbros, as
766 well as some of the medium-fine grained gabbros, exhibit ortho- to mesocumulate
767 textures. The contacts between individual gabbro bodies and the medium-fine
768 grained gabbro are gradational over 1 to 5 cm, exhibiting mingling textures and
769 inclusions of gabbros with contrasting textures (Fig S2, S3). These characteristics
770 suggest that the gabbros of the western limb accumulated from multiple pulses of
771 magma that supplied compositionally similar melts within a relatively short period
772 of time, such that previously intruded gabbroic magma was still partially molten to
773 allow for mingled and gradational contacts. Due to their close temporal
774 association, these pulses of magma likely originated from the same source, and are
775 therefore part of a cogenetic sequence. The presence of both liquid-like and
776 cumulate gabbros in the western limb suggest that the parental melts to the gabbros
777 continued to fractionate *in-situ*.

778 The southeastern section of the HLMC consists of a single large medium-
779 fine grained gabbro body containing norite and anorthosite cumulate pods, as well
780 as a lens of coarse-grained gabbro, but is overall more texturally homogenous than
781 the western section. The presence of well-defined cumulate textures in these rocks
782 indicates that separation of crystals and liquid occurred within the mafic complex.

39

783 The contacts between gabbros, monzodiorite, and monzonite in the northern and
784 northeastern section of the HLMC (Fig 1) are largely gradational over 5 to 10 m,
785 and there is no distinct contact between the medium-fine grained gabbros of the
786 western limb and this lithology in the eastern section. This suggests that eastern
787 HLMC and the western medium-fined grained gabbros were emplaced as a single
788 large intrusion that differentiated *in-situ* to create the norite and gabbro cumulates
789 and melt was extracted from the gabbros to produce the more evolved
790 monzodiorites and monzonites. This is consistent with petrographic observations
791 suggesting that most of the gabbros are meso- and adcumulates, with the exception
792 of three liquid-like gabbro samples.

793 The presence of both cumulate and liquid-like gabbros, monzodiorites, and
794 monzonites suggests that the gabbroic HLMC parental intrusions fractionated *in-*
795 *situ*. Multiple intrusions into the medium-fine grained gabbro are preserved as
796 gabbros with contrasting textures, and the bodies that represent separate intrusions
797 all have parental melts of similar composition. The gradational boundaries between
798 the gabbros and monzonitic lithologies, as well as evolved pods within the
799 gabbros, indicate that the evolved lithologies were generated by extraction of melt
800 from the gabbroic cumulates. While some melts may have been extracted to
801 shallower levels in the crust, the liquid-like compositions present in HLMC
802 represent melts generated by fractionation within HLMC.

40

803 Evidence for mixing between HLMC and felsic melts at the level of
804 emplacement is minimal and confined to the outer margins of the complex, and so
805 is unlikely to have caused the compositional variation within the mafic body.
806 Locally, the 90.5 to 96.5 Ma HLMC parental melts intruded into the much older
807 granite of Chickenfoot Lake (Jcf, 191.6 Ma), which would have been fully
808 crystallized prior to the mafic intrusions. Any volume of Jcf-derived felsic melt
809 would need to be produced by heat from HLMC intrusions. This effect is visible
810 along the HLMC-Jcf contact, where a dioritic gradational zone (Fig S3b) indicates
811 short-distance mixing between a HLMC parental melt and granitic melt produced
812 by partial melting of Jcf. However, this hybridized lithology does not extend more
813 than 1 m from the granite-gabbro contact. The contact between Kle and HLMC is
814 sharp and indicates little to no mixing or assimilation. Because Krv is younger than
815 HLMC, and HLMC-sourced blocks in the brecciated contact between these units
816 are angular with sharp contacts, HLMC was likely solidified by the time of Krv
817 intrusion and therefore could not mix. Field evidence precludes substantial magma
818 mixing origin for the compositional diversity within the HLMC and supports *in-*
819 *situ* fractional crystallization.
820

41

Geochemical Evidence

The HLMC compositional trends suggest that the various rock types are related to one another by fractional crystallization. Bulk-rock analyses preserve a wide range of SiO_2 contents from 43.6 to 61.5 wt.% (Fig 3). Bulk-rock Mg# decreases from 73.1 to 35.8, though a compositional gap exists between the norites and gabbros (Mg#= 57.8 to 64.6). Al_2O_3, TiO_2, CaO, MgO, and FeO contents are variable over approximately constant SiO_2 content in the norites, then smoothly decrease from the gabbros to monzodiorites to monzonites. Similar trends are present in K_2O and Na_2O, but their concentrations increase with increasing SiO_2 content. These compositional relationships are consistent with a fractional crystallization liquid line of descent (LLD) and associated cumulates in arc settings (Müntener and Ulmer 2018).

In general, incompatible trace element concentrations in liquid-like samples increase with increasing SiO_2 content, indicating enrichment of these elements in the remaining melt with progressive fractionation. Exceptions to this are Ni and Cr, which are are rapidly removed from the melt during norite crystallization, and Sr which decreases with increasing SiO_2 after saturation of significant amounts of plagioclase. HREE elements are depleted relative to LREE elements in all rock types (Fig 4), and this depletion, indicated by La/Yb ratio, increases with increasing SiO_2 content. Though there is significant overlap in the degree of HREE

42

841 depletion between rock types, this pattern nevertheless supports a fractional
842 crystallization origin for the HLMC lithologies.
843 Mineral compositions are also consistent with a cogenetic fractionation
844 sequence. Very similar trends are seen in ortho- and clinopyroxene, in which MnO
845 and Mg# are negatively correlated and higher Mg#s correspond to lithologies
846 crystallized earlier in the fractionation sequence. Cr_2O_3 and Al_2O_3 in orthopyroxene
847 (Fig 6b) decrease with decreasing Mg# and with increasing bulk-rock SiO_2 content,
848 indicating depletion of these components in the melt with olivine + pyroxene and
849 plagioclase fractionation. Euhedral plagioclase crystals in the norites have very
850 similar An content to the plagioclase cores in the gabbros and monzodiorites,
851 suggesting that these cores crystalized from a melt similar to the norite parental
852 melt and were progressively rimmed by lower-Ca plagioclase as the remaining
853 melt evolved. In biotite, the observed decreasing F (Fig 6d) and TiO_2 content with
854 decreasing Mg# correspond to increasing FeO content in the biotite and decreasing
855 crystallization temperature, respectively.
856 Thus, both the mineral compositions and modal mineralogy of the rocks indicate
857 derivation by fractional crystallization from a common parental melt defined by a
858 lithological progression of norites → gabbros → monzodiorites → monzonites and
859 a mineral crystallization sequence of olivine → orthopyroxene + amphibole(high-

860 Al) → clinopyroxene + Fe-Ti oxides → plagioclase + amphibole(low-Al) →
861 biotite → K-feldspar → quartz.
862
863 **Composition of the HLMC Parental Melt**
864 We define the HLMC parental melt as a representative, initial melt
865 composition that intruded into the upper crust at the location of HLMC and
866 fractionated to produce the range of observed lithologies. Based on our inferred
867 fractionation sequence, olivine is the first phase to crystallize from the parental
868 melt and is our best indicator of its composition. The most primitive analyzed
869 olivine core in HLMC has a Mg# of 81. We calculate the Mg# of the parental melt
870 coexisting with this olivine to be 51, using the olivine-melt distribution coefficient
871 of 0.32 (Blundy et al. 2020; Beattie 1993) and assuming an fO_2 of NNO and thus
872 Fe^{3+}/Fe^{T} ratio of 0.2 (Kress and Carmichael 1991).
873 Primitive lavas erupted at continental arcs are thought to be representative of
874 sub-arc mantle melts, and span a Mg# range of 67 to 73 based on a global
875 compilation by Schmidt and Jagoutz (2017). The Mg# of the HLMC parental melt
876 (51) is significantly lower than these values and therefore does not represent a
877 (non-modified) partial melt of the mantle, but rather one that has experienced prior
878 differentiation at deeper crustal levels. The major and trace element concentrations
879 (Cr, Ni, Rb, Sr, Y, Zr, Nb, Ba, REEs, Hf, Ta, Pb, Th, U) of the HLMC parental

44

880 melt are determined via fractionation modeling as discussed below, and included in
881 the Supplementary Data File (Table ST5). Though a basaltic dike exists in HLMC
882 that appears to be a potential parental melt composition based on major element
883 concentrations (SNB-14-39), this sample is significantly enriched in incompatible
884 trace elements (particularly Nb, Rb, La, Ce, Lu, Ta, and Th) relative to the liquid-
885 like samples at similar SiO_2 contents. Thus, we infer that this dike is not a parental
886 melt and prefer the calculated parental melt composition.
887
888 **Evidence for Lower Crustal Crystallization-Differentiation**
889 Although the SNB is dominated by felsic plutons that crystallized at shallow
890 pressures (generally <0.5 GPa; Nadin et al. 2016), direct evidence for deep crustal
891 processes is present as ultramafic to mafic Cretaceous xenoliths in Miocene to
892 Pliocene basalts in the central SNB, sourced from 1 to 3 GPa (Lockwood and
893 Bateman 1976; Peselnick et al. 1977; Domenick et al. 1983; Dodge et al. 1986;
894 Dodge et al. 1988; Mukhopadhyay 1991; Mukhopadhyay and Manton 1994; Ducea
895 and Saleeby 1996; Ducea and Saleeby 1998; Lee et al. 2001; Lee et al. 2006). In
896 addition, southern exposures of the batholith in the Tehachapi Mountains
897 crystallized at pressures between 0.7 to 1.0 GPa (Ross 1985; Sams and Saleeby
898 1988; Pickett and Saleeby 1993; Lackey et al. 2005; Saleeby et al. 2008; Klein and
899 Jagoutz 2021, Rezeau et al. 2021). Orthopyroxene compositions from lower crustal

garnet-pyroxenite cumulate xenoliths range from Mg# ~80 to 90 (Fig 6b; Dodge et al. 1986; Lee et al. 2006). Using the orthopyroxene-melt distribution coefficient of 0.284 (Beattie 1993) and assuming an fO_2 of NNO (as above), the orthopyroxene crystallized from melts ranging from a primitive mantle melt (Mg#= 69) to a fractionated basalt (Mg#= 48). These cumulates therefore record lower crustal differentiation and the generation of low-Mg basalts that are consistent with the HLMC parental melt composition. Additionally, the most primitive HLMC norite orthopyroxene compositions overlap with the least primitive compositions in the xenoliths (Mg# ~80), indicating that both cumulates crystallized from similarly fractionated melts.

Likewise, a lower crustal section of the southern SNB is exposed in the Tehachapi Mountains, and exposes depths of up to 30 km (~1.0 GPa) (Ague and Brimhall 1988; Pickett and Saleeby 1993). Within the Tehachapi Complex, the Bear Valley Intrusive suite (BVIS, 0.4-1.0 GPa) consists of tonalite, norites, and hornblende gabbros (Klein and Jagoutz 2021). The mineralogical similarities between the gabbroic cumulate rock types of the BVIS and the HLMC mafic cumulates, particularly the prevalence of amphibole and orthopyroxene, suggest that the melts that intruded into the upper crust are compositionally similar to those that crystallized in the SNB mid-lower crust. Additionally, the most primitive bulk rock analysis of gabbroid cumulates from the BVIS (Mg#=73.4; Klein and Jagoutz

46

2021) is similar to the most primitive HLMC norite (Mg#=73.1), suggesting that the parental melts to both intrusions were similarly evolved basalts. Thus the parental melts to both the BVIS and the HLMC may be generated by the same process, namely through deeper crustal differentiation as recorded by the ultramafic xenoliths.

In our case study of HLMC, differentiation of a primitive basalt is required prior to the intrusion of the low-Mg parental melt in the upper crust. We favor lower crustal fractional crystallization over partial melting of underplated basalts as thermal modeling studies demonstrate that this latter process is more likely to produce more silicic rather than basaltic or basaltic-andesite compositions (Annen et al. 2006; Jagoutz and Klein 2018). Remaining possibilities for generating an evolved basaltic melt include assimilation of felsic crust by a primitive basalt or direct fractionation from a primitive basalt in the lower, mid- or upper crust. Assimilation of crustal material is highly unlikely to produce the HLMC parental melt composition from a mantle melt because assimilation of enough crustal melt to decrease the basalt Mg# from ~70 to 51 would significantly increase the melt SiO_2 content. Mid- and upper crustal fractionation of large volumes of primitive melts is improbable because ultramafic cumulates are rarely observed at these depths in the SNB. We therefore infer that the initial stage of fractional

47

939 crystallization occurred in the lower crust within the range of cumulate-dominated
940 lithologies, as observed in accreted arc sections.
941
942 **Polybaric Fractionation Model**
943 Field relationships and geochemistry indicate that the HLMC lithologies
944 may be related by a common liquid line of descent (LLD) produced via fractional
945 crystallization, and their trace element signatures indicate that parental melts were
946 likely sourced from a sub-arc mantle melt. However, as discussed above, this
947 parental melt was fractionated relative to a primitive mantle melt. Thus,
948 fractionation must have occurred prior to the intrusion of the HLMC parental melts
949 at their current level in the crust (~0.3 GPa) where further differentiation occurred.
950 In agreement with studies of polybaric fractionation in arcs (Almeev et al. 2013;
951 Hamada et al. 2014; Melekhova et al. 2015), we construct a two-stage fractionation
952 model to test our fractional crystallization hypothesis. Stage 1 models fractional
953 crystallization of a primitive mantle melt in the lower arc crust using cumulate
954 compositions of xenoliths crystallized at depths of >30 km (Lee et al. 2006) to
955 produce a low-MgO basalt that becomes the parental melt to HLMC. Stage 2
956 tracks fractionation of this evolved basalt in the upper crust by removal of analyzed
957 cumulate compositions from the HLMC from an evolving modeled liquid
958 composition. It is conceivable that multiple episodes of fractionation could have

959 occurred prior to Stage 2 at different levels in the crust below 0.3 GPa. However,
960 we choose the simplest approach and assume only one stage of crystallization prior
961 to intrusion at the level of HLMC exposure. The LLDs generated from our
962 modeling are illustrated in Figure 7, as well as Figures S10 and S11, and all results
963 of modeling calculations are included in the Supplementary Data File (Tables S4-
964 S6).
965
966 *Stage 1: Lower Crustal Fractionation Model Description*
967 We model the evolution of a sub-arc mantle-derived melt by progressive
968 removal of bulk cumulate compositions from a melt composition, following the
969 methods of Jagoutz (2010). In this initial deep-crustal phase of differentiation, we
970 use representative compositions of cumulate xenoliths (Table S4) that crystallized
971 in the SNB lower crust between 1 and 3 GPa (Dodge et al. 1986; Lee et al. 2006),
972 using a fractionation sequence of orthopyroxenite and websterite → garnet-
973 pyroxenite. The starting melt composition was varied within the range of primitive
974 basalts from the Andes, Cascades, Central American, Mexican, and New Zealand
975 continental arcs (Schmidt and Jagoutz 2017). Stage 1 fractionation produces a
976 fractionated melt in equilibrium with the most primitive cumulates in HLMC at the
977 end of the Stage 1 and most successfully reproduces the HLMC liquid-like
978 compositions when input into the Stage 2 model. Stage 1 lower crustal

49

979 fractionation proceeds until the remaining melt reaches an Mg# of 51 after 33%
980 crystallization, in equilibrium with the most primitive minerals in HLMC.
981 Because comprehensive trace element concentrations are not available for
982 all xenolith lithologies, we also model Stage 1 fractional crytallization using
983 alphaMELTS (Ghiorso and Sack 1995; Asimow and Ghiorso 1998) to generate a
984 trace element profile for the HLMC parental melt. A crystallization pressure of 1.1
985 GPa, or ~35 km depth, was used to replicate the lower crust of the Sierra Nevada
986 arc as predicted by seismic studies (Jones and Phinney 1998; Ruppert et al. 1998;
987 Fliedner et al. 2000). Following our best estimates for oxygen fugacity, we
988 performed models at NNO. Initial water contents were assumed to be 2 wt.% H_2O,
989 which is within the range of primitive (Mg#= 65-74) melt inclusion concentrations
990 from basalts in the Mexican, Cascade, and Kamchatkan arcs (1.0-5.2 wt.% H_2O;
991 Sisson and Layne 1993; Cervantes and Wallace 2003; Portnyagin et al. 2007) and
992 reproduces the H_2O content (2.9-3.5 wt.%) of the HLMC gabbros after completion
993 of Stage 1 crystallization. Though the xenolith-based and alphaMELTS models
994 produce the HLMC parental melt composition from slightly different primitive
995 starting compositions and diverge after the melt reaches the HLMC parental melt
996 composition, the orthopyroxenite and clinopyroxenite cumulates produced by the
997 MELTS model are consistent with xenolith compositions from the SNB lower
998 crust (Fig 7). After generation of the HLMC parental melt, we extend both the

xenolith fractionation and MELTS models to Mg#<51 to assess the melt evolution had it not been extracted from the lower crust (shown as dashed lines in Fig 7), but this is not included in our polybaric crystallization model.

Stage 2: Upper Crustal Fractionation Model Description

We use a similar stepwise cumulate subtraction approach to model the LLD of the HLMC parental melt as it fractionally crystallizes in the upper crust. Average cumulate compositions are calculated for 6 representative lithologies from HLMC (Table S5) following the fractionation sequence discussed above. The starting liquid composition is the HLMC parental melt as generated by our lower crustal fractionation model. We do not use alphaMELTS to model this stage for two reasons: 1) amphibole is a common fractionating phase in the HLMC and alphaMELTS currently lacks an amphibole model that accurately reproduces observed phase assemblages from experimental and natural studies, and 2) the fractionating assemblage and cumulate compositions can be constrained from field and geochemical observations.

Proportions of Cumulates Crystallized

Cumulate assemblages are introduced to the fractionation sequence based on the calculated Mg# of melts in equilibrium with orthopyroxene and clinopyroxene

51

1019 in the lower-crustal xenoliths, determined using mineral-melt Mg-Fe distribution
1020 coefficients of 0.284 and 0.23, respectively (Beattie 1993; Sisson and Grove 1993).
1021 Because the garnet-pyroxenite xenoliths span a significant range in bulk-rock Mg#
1022 (39-83), we split this lithology into four fractionating cumulate groups to more
1023 accurately replicate crystallization from an evolving melt: group A (Mg# 80.5-83),
1024 group B (Mg# 74-80), group C (Mg# 62-68), and group D (Mg# 39-59).
1025 Compositions of cumulates used in this model are averages for each group, and are
1026 included in the Supplementary Data File. Fractionation of a primitive arc basalt
1027 during Stage 1 fractionation of lower crustal cumulates produces 16.6% (by mass)
1028 of orthopyroxenite (± clinopyroxene), 10.2% of group A garnet-pyroxenites, 7.0%
1029 of group B garnet-pyroxenites, and 0.6% of group C garnet-pyroxenites. At this
1030 point, the melt reaches an Mg# of 51 and ascends into the upper crust where the
1031 HLMC cumulates begin to crystallize. Stage 1 differentiation results in 33% total
1032 crystallization of cumulates (by mass), closely replicated by 33% crystallization of
1033 pyroxenites produced in the alphaMELTS model. The resulting liquid composition
1034 is input into the Stage 2 model as the HLMC parental melt.
1035 In accordance with our inferred fractionation sequence, low-Ca norites are
1036 the first cumulates to crystallize in Stage 2 (3% crystallization of the remaining
1037 melt mass), followed by high-Ca norite fractionation (9.3%), and low-SiO_2 gabbro
1038 crystallization (53%). As clino- and orthopyroxenes are consistently exsolved in

1039 the gabbros they are unlikely to record the equilibrium melt composition, and we
1040 therefore infer that the Mg# of the melt was between that of the low-SiO_2 (Mg#=
1041 46) and liquid-like gabbros (Mg#= 49) at the onset of high-SiO_2 gabbro
1042 crystallization. High-SiO_2 gabbro is assumed to crystallize until the liquid-like
1043 monzonite compositions are replicated at 63 wt.% SiO_2 (20% crystallization by
1044 mass). Fractionation of cumulate monzodiorites continues from 63 wt.% SiO_2 and
1045 Mg# 44.7 to 70 wt.% SiO_2 and Mg# 40 (7.3% by mass). Cumulate monzonites
1046 then fractionate until SiO_2 reaches 78 wt.% (2.9% by mass), near the maximum for
1047 granites in the SNB.
1048
1049 **Model Results**
1050 Our polybaric fractionation model reproduces the range of major and trace
1051 element compositions of the HLMC, and when extended to higher SiO_2 contents is
1052 capable of replicating the compositional trends defined by the SNB felsic plutons
1053 (63-78 wt.% SiO_2, Fig 7). In Stage 1, differentiated melts in equilibrium with the
1054 most primitive HLMC minerals are produced by 33% fractionation by mass of a
1055 primitive arc basalt at pressures between 1 and 3 GPa (>30 km). The resulting melt
1056 composition is the HLMC parental melt, which has an H_2O content of 3.3 wt.%
1057 consistent with our estimates from plagioclase hygrometry in the liquid-like
1058 gabbros. During this crystallization stage, the Mg# of the melt drops from 68 to 51

1059 with little change in SiO_2 (49.9 to 48.9 wt.%) due to significant fractionation of
1060 orthopyroxene and clinopyroxene, with lesser contributions from garnet. Initially,
1061 16.6% by mass of orthopyroxenite (with minor websterite) crystallizes, causing a
1062 decrease in Mg# from 68 to 59 (Fig 7a). Over this interval, MgO in the remaining
1063 melt decreases from 11.8 to 8.4 wt.%, while all other major oxides increase
1064 accordingly and ASI remains stable at 0.64. Garnet-pyroxenites (group A, Mg#
1065 80.5-83) begin to fractionate at a melt Mg# of 59, in equilibrium with the highest
1066 Mg# clinopyroxene (Mg#= 65, Fe-Mg distribution coefficient 0.23; Sisson and
1067 Grove 1993). 10.2% of the melt crystallizes to form group A garnet-pyroxenites,
1068 causing an increase in melt ASI from 0.64 to 0.71 and decrease in Mg# from 59 to
1069 55. Following, 6.3% resulting in a melt Mg# of 51 and ASI of 0.74. At this point,
1070 the melt is in equilibrium with the most primitive HLMC minerals. If the melt were
1071 to remain in the lower crust, the group C and D garnet-pyroxenites would proceed
1072 to crystallize, causing ASI to further increase, as is described below. Within Stage
1073 1 crystallization, the MgO content of the melt decreases from 11 to 6.2 wt.% with a
1074 concurrent increase in FeO from 10 to 10.6 wt.%. This crystallization also causes a
1075 significant increase in Al_2O_3 from 13.5 to 17.2 wt.% with only a slight increase in
1076 CaO (9.4 to 10 wt.%), driving the observed rise in ASI.

1077 The derivative basalt produced at the end of Stage 1 is assumed to
1078 subsequently ascend, intrude into the upper crust, and further differentiate. The

1079 removal of norite cumulates, dominated by orthopyroxene with minor olivine and
1080 plagioclase, drives an initial decrease in the melt Mg# from 51 to 47 at relatively
1081 steady SiO_2. CaO, Al_2O_3, Na_2O, and Sr content increase in the melt during this
1082 interval due to the paucity of accumulated feldspar in the norites.

1083 Following the onset of low-SiO_2 gabbro crystallization, MgO, CaO, FeO,
1084 and TiO_2 smoothly decrease through the remaining LLD, while K_2O, ASI, and
1085 incompatible trace elements consistently increase. Fractionation of the low-SiO_2
1086 gabbros causes a significant increase in the melt SiO_2 content from 49.9 to 56
1087 wt.%. The low SiO_2 (43.9-46.8 wt.%) and high FeO and TiO_2 (9.6-13.6 and 1.2-1.6
1088 wt.%, respectively) content of the low-SiO_2 gabbros is due to abundant amphibole
1089 and Fe-Ti oxides. As such, fractionation of these cumulates drives the SiO_2
1090 enrichment and FeO and TiO_2 decrease in the melt. The liquid also decreases in
1091 MgO and CaO content over this fractionation interval. In contrast to norite
1092 fractionation, plagioclase is now a major fractionating phase and the Al_2O_3 content
1093 of the melt increases only slightly during low-SiO_2 gabbro fractionation, from 18.2
1094 to 18.5 wt.%. Na_2O and P_2O_5 increase due to crystallization of high-Ca plagioclase
1095 ($\sim An_{80}$) and a lack of apatite in the low-SiO_2 gabbros.

1096 High-SiO_2 gabbro fractionation continues the trend of increasing SiO_2
1097 content (56-63 wt.%) with a limited decrease in Mg# (47 to 45). Plagioclase is
1098 abundant in these cumulates and has lower An content ($\sim An_{50}$) than in the low-

1099 SiO_2 gabbros, causing Al_2O_3 to decrease and the rate of Na_2O increase to shallow.
1100 Al_2O_3, Na_2O, and P_2O_5 content continue to decrease for the remainder for the LLD.
1101 When gabbro fractionation ceases, the model has reproduced the most fractionated
1102 liquid-like monzonite in HLMC with 16.2% of the mass of HLMC parental melt
1103 remaining, or 10.9% for the primitive arc basalt.

1104 Fractionation of monzordiorite cumulates from the remaining melt continues
1105 the increasing trends in SiO_2 (63-71 wt.%), K_2O (3.0-4.5 wt.%), and Na_2O (3.5-3.7
1106 wt.%). The melt Mg# decreases from 45 to 40, along with decreasing MgO, TiO_2,
1107 and FeO primarily due to amphibole and biotite crystallization, and decreasing
1108 CaO and Al_2O_3 which are depleted by plagioclase and amphibole fractionation.
1109 This crystallization interval replicates a representative SNB granodiorite
1110 composition (67.5 wt.% SiO_2, Table S5) with 9.9% of the parental melt and 6.6%
1111 of the primitive melt masses remaining. Monzonite fractionation continues the
1112 monzodiorite fractionation trends, causing the evolving melt composition to
1113 increase from 71 to 75 wt.% SiO_2. Mg# notably decreases from 40 to nearly 0 as
1114 MgO is consumed by fractionating amphibole and biotite. At this point, the
1115 remaining granitic melt mass is 5.8% of the HLMC parental melt and 3.9% of the
1116 primitive arc basalt.

1117 To determine if the HLMC evolved rocks and SNB granodiorites could be
1118 produced by continued lower crustal fractionation, we extend both the lower

crustal (xenolith) crystallization model and the alphaMELTS model to Mg#s<51 (Fig 7). Though the starting compositions we use are within the low range of Al_2O_3 values found in primitive arc basalts (<13.5 wt. % Al_2O_3) (Schmidt and Jagoutz 2017), our models of lower crustal fractionation always produce peraluminous andesite liquids (i.e., ASI>1.1 when SiO_2<57 wt.%). In our model and in the Blatter et al. (2013) experiments, plagioclase does not become a significant fractionating phase at >0.9 GPa until 33 to 30% of the initial melt mass is remaining. In the xenolith cumulate crystallization model, Al is initially removal from the melt by minor incorporation into orthopyroxene and has little effect on ASI. Garnet is included in the fractionating cumulates after 17% crystallization, but the group A and B garnet-pyroxenites have low Al_2O_3 contents (7.6-8.8 wt.%) relative to CaO (12.1-15.7 wt.%), leading to a continuous increase in ASI. Thus, the HLMC compositions and non-peraluminous evolved arc melts are inconsistent with extensive lower crustal fractionation.

Comparison to Other Upper Crustal Mafic Bodies in the SNB

Numerous mafic bodies are preserved in the SNB upper crust and several have been investigated for geochronology and geochemistry (Frost 1987; Frost and Mahood 1987; Coleman et al 1995; Sisson et al. 1996; Ratajeski et al. 2001; Holland et al. 2013). The Onion Valley (92.1 ± 0.3 Ma), Armstrong Canyon (91.5

1139 ± 0.1 Ma), and Lake Sabrina (91.1 ± 0.3 Ma) mafic complexes in the eastern Sierra
1140 Nevada (Coleman et al. 1995) are broadly coeval with HLMC (90.5-96.5 Ma).
1141 Mafic magmatism in all four localities was contemporaneous with voluminous late
1142 Cretaceous felsic intrusions throughout the Sierra Nevada arc (Ducea 2001),
1143 demonstrating that mafic and felsic magmatism was coeval and possibly cogenetic.
1144 Geochemical data from the lower crustal Bear Valley Intrusive Suite (Klein
1145 and Jagoutz 2021) and 10 upper crustal SNB mafic complexes in addition to
1146 HLMC are presented in Figure 8. All localities are in the eastern SNB from Frost
1147 (1987) and Sisson et al. (1996) except for the Yosemite samples of Ratajeski et al.
1148 (2001) and the Ash Mountain complex of Holland et al. (2013). Amphibole-
1149 gabbros (± olivine) and amphibole-bearing diorites are common throughout the
1150 mafic complexes, indicative of crystallization from hydrous parental melts. In
1151 particular, the parental melt to the Onion Valley complex is estimated to have 6
1152 wt.% H_2O (Sisson et al. 1996). The most primitive cumulates in the Onion Valley
1153 complex are olivine-hornblendites and the intrusion is generally pyroxene-poor.
1154 This is in contrast to the orthopyroxene-dominated norites of HLMC, which
1155 indicate crystallization from a less hydrous parental melt (estimated 3.1 wt.%
1156 H_2O). In both cases, elevated water contents likely facilitate the ascent of the low-
1157 Mg, high-Al basalts into the upper crust due to their decreased density and
1158 viscosity (Sisson et al. 1996).

58

1159 Layered cumulates and internal compositional ranges from gabbro to diorite
1160 within each body (Frost 1987; Sisson et al. 1996; McCarthy and Müntener 2016)
1161 suggest that *in-situ* upper crustal fractionation is common in upper crustal mafic
1162 complexes. Olivines from the Onion Valley complex have a maximum Mg# of
1163 81.7 (in equilibrium with melt Mg# = 52), and sheeted sills interpreted as
1164 representative of melt compositions have Mg#s ranging from 41 to 54.5 (Sisson et
1165 al. 1996). The most primitive sill and the olivine-melt estimates are slightly more
1166 primitive, but still comparable to the HLMC parental melt (Mg# = 51), suggesting
1167 that the parental melts to these two bodies were fractionated to a similar degree in
1168 the lower crust prior to ascent. Mineral chemistry only exists for the Onion Valley
1169 and Hidden Lakes mafic complexes, rendering it is difficult to calculate the Mg# of
1170 parental melts for the other complexes. However, maximum bulk-rock Mg#s in
1171 each complex range from 53 to 76.5, and therefore did not fractionate from a
1172 primitive basalt (Mg# of cumulates > 80). Thus lower crustal differentiation is
1173 required to generate low-Mg basalts in order to produce these upper crustal mafic
1174 intrusions. Derivation of the upper crustal mafic complexes from evolved basalts
1175 and the presence of upper crustal cumulate lithologies demonstrate that polybaric
1176 fractionation is a common process in generating the range of compositions in SNB
1177 mafic complexes.

59

All mafic complex samples have ASI values less than 1, indicating that the mafic melts that escape the lower crust are generally not peraluminous. Samples with high ASI relative to their SiO_2 content (ASI = ~0.8-0.97, SiO_2= 40.7-50.3 wt.%) are likely cumulates, and thus reflect plagioclase accumulation rather than parental melts with initially high ASI values. Lower crustal fractionation of a primitive arc basalt creates peraluminous melts at 51 wt.% SiO_2 (our model) to 56 wt.% SiO_2 (Blatter et al. 2013) by ~55% crystallization. Thus, melts that generate the mafic complexes must escape the lower crust (>0.7 GPa) before evolving to andesitic compositions. Because some lithologies found in these complexes have SiO_2 > 56 wt.%, upper crustal differentiation must occur to create these compositions after extraction from the lower crust.

Though mineral compositional data is limited to two complexes, those that do exist define a narrow range of parental melt compositions (Mg# = 51-54.5). The range of bulk-rock cumulate compositions from other complexes are similar in Mg# to the Onion Valley and Hidden Lakes mafic complexes, suggesting that all upper crustal mafic complexes may be derived from melts that are fractionated to a similar degree in the lower crust. Additionally, the SiO_2 content of hydrous parental melts cannot exceed 56 wt.% without becoming peraluminous during fractional crystallization at >0.7 GPa. Therefore, we suggest that there may be a narrow window of rheologic properties that allow these hydrous basalts to ascend.

60

For example, the hydrous, but still relatively low-SiO_2 nature of these basalts reduces their viscosity and decreases their density, enhancing their ability to ascend via diking (Sisson et al. 1996).

Production of Sierra Nevada Batholith Granitoids

Our polybaric fractionation model results support the hypothesis that the HLMC is an example of upper crustal fractional crystallization of a low-Mg basalt in a continental arc and that lower crustal fractionation is required to produce the HLMC parental basalt. We show that arc-like granodiorite and granite compositions can be generated by this two-stage crystallization process and thus polybaric crystallization can contribute to the generation of non-peraluminous granitoids in the SNB. However, volumes of mafic (noritic to gabbroic) cumulates at upper crustal depths (0.1-0.4 GPa) are relatively small. We posit that the fractionation of a low-MgO basalt deeper than the exposures of much of the SNB, yet at depths sufficiently low to allow for plagioclase saturation (<0.7 GPa), could generate evolved non-peraluminous melts. Crystallization of "damp" basalt to andesitesand enhancement of orthopyroxene stability could also contribute to limiting the increase in ASI of differentiating melts at high pressures (Rezeau et al., 2021). This is supported by gabbro and gabbronorite lithologies with a maximum Mg# identical to the HLMC (Mg# = 73) in the ~0.8-0.9 GPa section of

61

1218 the Bear Valley Intrusive Suite (BVIS; Klein and Jagoutz 2021). Because the BVIS
1219 lithologies did not crystallize from a primitive mantle melt, an initial stage of
1220 fractionation is required below ~1 GPa, analogous to Stage 1 in our model for the
1221 HLMC. Throughout the batholith, Stage 2 fractionation may occur below
1222 exposures of the bulk of the SNB (>0.4 GPa) to produce granodioritic melts
1223 consistent with SNB compositions, which proceed to intrude into the upper crust.
1224 This reconciles the discrepancy between experimental and observational data, in
1225 which experiments indicate that melts produced by lower crustal fractionation
1226 rapidly become peraluminous (Cawthorn and Brown 1976; Cawthorn and O'Hara
1227 1976; Blatter et al. 2013; Nandedkar et al. 2014; Müntener and Ulmer 2018; Ulmer
1228 et al. 2018), yet lower crustal ultramafic cumulates are ubiquitous in arc crustal
1229 cross sections (Debari and Sleep 1991; Greene et al. 2006; Otamendi et al. 2012;
1230 Jagoutz 2014; Walker et al. 2015; Guo et al. 2020). HLMC has captured a local
1231 example of upper crustal differentiation, indicating that granodiorite compositions
1232 consistent with the SNB can be produced by a polybaric fractionation processes
1233 with a range of possible depths for fractionation of a low-MgO basalt.

1234 The volumes of intermediate to evolved (>60 wt.% SiO_2) melt produced by
1235 fractional crystallization will be small compared to the volumes of cumulates, so
1236 polybaric crystallization may not be the only mechanism for the generation of arc
1237 granodioites. Previously proposed mixing models for the SNB (e.g., Reid et al.

62

1983; Frost and Mahood 1987; Sisson et al. 1996), require both a high-SiO_2 melt, and an evolved basalt similar to the HLMC parental melt. Although the mechanical viability of mixing felsic and mafic melts is limited, these models also resolve the problem of peraluminous melt compositions generated by lower crustal fractionation, because the homogenized products between non-peraluminous, low-Mg basalts and mildly peraluminous (i.e, ASI<1.1) granitic melts are consistent with batholith granitoid compositions (Blatter et al. 2013). Our modeling identifies a potential low-Mg basaltic end member composition (the HLMC parental melt) produced by lower crustal fractionation. We show that evolved basalts must be generated in the lower crust, and are thus available to participate in both mixing and polybaric crystallization proceses that contribute to the production of batholith-scale volumes of granodiorite.

Conclusions

The Late Cretaceous Hidden Lakes mafic complex is a preserved example of intrusion of melt into the upper crust of the Sierra Nevada batholith contemporaneously with more voluminous felsic magmas. Bulk-compositions of lithologies ranging from olivine-norites to monzonites are consistent with fractional crystallization from a moderately hydrous basalt (2.9-3.5 wt% H_2O) at ~0.3 GPa, and oxidizing conditions (~NNO). The parental melt to the HLMC is a

low-Mg basalt produced through differentiation in the lower crust prior to intruding into the upper crust.

We model this polybaric fractional crystallization process in two-stages, using cumulate compositions from SNB deep crustal xenoliths, accompanied by alphaMELTS, to calculate the composition of an evolving primitive arc basalt in the lower crust (Stage 1) and constructing an upper crustal fractionation based on measured cumulate and liquid-like sample compositions (Stage 2). Our model indicates 33% mass fractionation in the lower crust, followed by extraction to upper crustal pressures and subsequent fractionation to form all HLMC cumulates and melt compositions. Polybaric fractionation of mantle-derived basalt to produce granodiorite resolves the disagreement between the prevalence of lower crustal cumulates in arcs and experimental data that suggest lower crustal fractionation will produce peraluminous melts inconsistent with arc batholith compositions.

The HLMC contains rock types that are lithologically and compositionally similar to those other upper crustal mafic complexes of the SNB, suggesting that these intrusions crystallized from hydrous, fractionated basalts of comparable compositions. Consequently, their composition may be governed by unifying rheologic characteristics that facilitate their ascent from the lower crust such as reduced density and viscosity.

64

References

Ague JJ, Brimhall GH (1988) Magmatic arc asymmetry and distribution of anomalous plutonic belts in the batholiths of California: Effects of assimilation, crustal thickness, and depth of crystallization. Geological Society of America Bulletin 100(6):912-927

Almeev RR, Ariskin AA, Kimura J-I, Barmina GS (2013) The role of polybaric crystallization in genesis of andesitic magmas: phase equilibria simulations of the Bezymianny volcanic subseries. Journal of Volcanology and Geothermal Research 263:182-192

Annen C, Blundy J, Sparks R (2006) The genesis of intermediate and silicic magmas in deep crustal hot zones. Journal of Petrology 47(3):505-539

Arai S, Ishimaru S (2008) Insights into petrological characteristics of the lithosphere of mantle wedge beneath arcs through peridotite xenoliths: a review. Journal of Petrology 49(4):665-695

Asimow PD, Ghiorso MS (1998) Algorithmic modifications extending MELTS to calculate subsolidus phase relations. American Mineralogist 83(9-10):1127-1132

Bartels KS, Kinzler RJ, Grove TL (1991) High pressure phase relations of primitive high-alumina basalts from Medicine Lake volcano, northern California. Contributions to Mineralogy and Petrology 108(3):253-270

Bas ML, Maitre RL, Streckeisen A, Zanettin B, Rocks ISotSoI (1986) A chemical classification of volcanic rocks based on the total alkali-silica diagram. Journal of petrology 27(3):745-750

Bateman PC (1992) Pre-Tertiary bedrock geologic map of the Mariposa 1° by 2° quadrangle, Sierra Nevada, California; Nevada. The Survey,

Bateman PC, Eaton JP (1967) Sierra Nevada Batholith: The batholith was generated within a synclinorium. Science 158(3807):1407-1417

Blatter DL, Sisson TW, Hankins WB (2013) Crystallization of oxidized, moderately hydrous arc basalt at mid-to lower-crustal pressures: implications for andesite genesis. Contributions to Mineralogy and Petrology 166(3):861-886

Beattie P (1993) Olivine-melt and orthopyroxene-melt equilibria. Contributions to Mineralogy and Petrology 115(1):103-111

Blundy JD, Holland TJ (1990) Calcic amphibole equilibria and a new amphibole-plagioclase geothermometer. Contributions to mineralogy and petrology 104(2):208-224

Blundy J, Melekhova E, Ziberna L, Humphreys MC, Cerantola V, Brooker RA, McCammon CA, Pichavant M, Ulmer P (2020) Effect of redox on Fe–Mg–Mn exchange between olivine and melt and an oxybarometer for basalts.

Contributions to mineralogy and petrology 175(11):1-32
Brounce M, Kelley K, Cottrell E (2014) Variations in Fe3+/∑ Fe of Mariana Arc basalts and mantle wedge f O2. Journal of Petrology 55(12):2513-2536
Bucholz CE, Jagoutz O, Schmidt MW, Sambuu O (2014) Fractional crystallization of high-K arc magmas: biotite-versus amphibole-dominated fractionation series in the Dariv Igneous Complex, Western Mongolia. Contributions to Mineralogy and Petrology 168(5):1072
Bucholz CE, Spencer CJ (2019) Strongly Peraluminous Granites across the Archean–Proterozoic Transition. Journal of Petrology 60(7):1299-1348
Bucholz CE, Stolper EM, Eiler JM, Breaks FW (2018) A comparison of oxygen fugacities of strongly peraluminous granites across the Archean–Proterozoic boundary. Journal of Petrology 59(11):2123-2156

Cawthorn RG, Brown PA (1976) A model for the formation and crystallization of corundum-normative calc-alkaline magmas through amphibole fractionation. The Journal of Geology 84(4):467-476
Cawthorn RG, O'Hara MJ (1976) Amphibole fractionation in calc-alkaline magma genesis. American Journal of Science 276(3):309-329
Cervantes P, Wallace PJ (2003) Role of H2O in subduction-zone magmatism: new insights from melt inclusions in high-Mg basalts from central Mexico. Geology 31(3):235-238
Chapman AD, Saleeby JB, Wood DJ, Piasecki A, Kidder S, Ducea MN, Farley KA (2012) Late Cretaceous gravitational collapse of the southern Sierra Nevada batholith, California. Geosphere 8(2):314-341
Chapman JB, Gehrels GE, Ducea MN, Giesler N, Pullen A (2016) A new method for estimating parent rock trace element concentrations from zircon. Chemical Geology 439:59-70
Christensen NI, Mooney WD (1995) Seismic velocity structure and composition of the continental crust: A global view. Journal of Geophysical Research: Solid Earth 100(B6):9761-9788
Coleman D, Glazner A, Miller J, Bradford K, Frost T, Joye J, Bachl C (1995) Exposure of a Late Cretaceous layered mafic-felsic magma system in the central Sierra Nevada Batholith, California. Contributions to Mineralogy and Petrology 120(2):129-136
Debari S, Kay SM, Kay R (1987) Ultramafic xenoliths from Adagdak volcano, Adak, Aleutian Islands, Alaska: deformed igneous cumulates from the Moho of an island arc. The Journal of Geology 95(3):329-341
Debari SM, Sleep NH (1991) High-Mg, low-Al bulk composition of the Talkeetna island arc, Alaska: Implications for primary magmas and the nature of arc crust. Geological Society of America Bulletin 103(1):37-47

DeCelles PG, Ducea MN, Kapp P, Zandt G (2009) Cyclicity in Cordilleran orogenic systems. Nature Geoscience 2(4):251-257

Dodge F, Calk L, Kistler R (1986) Lower crustal xenoliths, Chinese Peak lava flow, central Sierra Nevada. Journal of Petrology 27(6):1277-1304

Dodge F, Lockwood J, Calk L (1988) Fragments of the mantle and crust from beneath the Sierra Nevada batholith: Xenoliths in a volcanic pipe near Big Creek, California. Geological Society of America Bulletin 100(6):938-947

Domenick MA, Kistler RW, Dodge F, Tatsumoto M (1983) Nd and Sr isotopic study of crustal and mantle inclusions from the Sierra Nevada and implications for batholith petrogenesis. Geological Society of America Bulletin 94(6):713-719

Draper DS, Johnston AD (1992) Anhydrous PT phase relations of an Aleutian high-MgO basalt: an investigation of the role of olivine-liquid reaction in the generation of arc high-alumina basalts. Contributions to Mineralogy and Petrology 112(4):501-519

Ducea M, Saleeby J (1998) A case for delamination of the deep batholithic crust beneath the Sierra Nevada, California. International Geology Review 40(1):78-93

Ducea MN (2001) The California arc: Thick granitic batholiths, eclogitic residues, lithospheric-scale thrusting, and magmatic flare-ups. GSA today 11(11):4-10

Ducea MN, Paterson SR, DeCelles PG (2015) High-volume magmatic events in subduction systems. Elements 11(2):99-104

Ducea MN, Saleeby JB (1996) Buoyancy sources for a large, unrooted mountain range, the Sierra Nevada, California: Evidence from xenolith thermobarometry. Journal of Geophysical Research: Solid Earth 101(B4):8229-8244

English JM, Johnston ST, Wang K (2003). Thermal modelling of the Laramide orogeny: testing the flat-slab subduction hypothesis. Earth and Planetary Science Letters *214*(3-4):619-632

Erdmann M, Koepke J (2016) Silica-rich lavas in the oceanic crust: experimental evidence for fractional crystallization under low water activity. Contributions to Mineralogy and Petrology 171(10):83

Fliedner MM, Klemperer SL, Christensen NI (2000) Three-dimensional seismic model of the Sierra Nevada arc, California, and its implications for crustal and upper mantle composition. Journal of Geophysical Research: Solid Earth 105(B5):10899-10921

Frost TP (1987) Sample localities, radiometric ages, descriptions, and major-and trace-element abundances of Late Jurassic mafic plutonic rocks, eastern

Sierra Nevada, California. Department of the Interior, US Geological Survey,

Frost TP, Mahood GA (1987) Field, chemical, and physical constraints on mafic-felsic magma interaction in the Lamarck Granodiorite, Sierra Nevada, California. Geological Society of America Bulletin 99(2):272-291

Gehrels GE, Valencia VA, Ruiz J (2008) Enhanced precision, accuracy, efficiency, and spatial resolution of U-Pb ages by laser ablation–multicollector–inductively coupled plasma–mass spectrometry. Geochemistry, Geophysics, Geosystems 9(3)

Ghiorso MS, Sack RO (1995) Chemical mass transfer in magmatic processes IV. A revised and internally consistent thermodynamic model for the interpolation and extrapolation of liquid-solid equilibria in magmatic systems at elevated temperatures and pressures. Contributions to Mineralogy and Petrology 119(2-3):197-212

Greene AR, DeBari SM, Kelemen PB, Blusztajn J, Clift PD (2006) A detailed geochemical study of island arc crust: the Talkeetna arc section, south–central Alaska. Journal of Petrology 47(6):1051-1093

Grove TL, Elkins-Tanton LT, Parman SW, Chatterjee N, Müntener O, Gaetani GA (2003) Fractional crystallization and mantle-melting controls on calc-alkaline differentiation trends. Contributions to Mineralogy and Petrology 145(5):515-533

Guo L, Jagoutz O, Shinevar WJ, Zhang HF (2020) Formation and composition of the Late Cretaceous Gangdese arc lower crust in southern Tibet. Contributions to Mineralogy and Petrology 175:58

Hamada M, Fujii T (2008) Experimental constraints on the effects of pressure and H 2 O on the fractional crystallization of high-Mg island arc basalt. Contributions to Mineralogy and Petrology 155(6):767-790

Hamada M, Okayama Y, Kaneko T, Yasuda A, Fujii T (2014) Polybaric crystallization differentiation of H 2 O-saturated island arc low-K tholeiite magmas: a case study of the Izu-Oshima volcano in the Izu arc. Earth, Planets and Space 66(1):1-10

Holland JE, Surpless B, Smith DR, Loewy SL, Lackey JS (2013) Intrusive history and petrogenesis of the Ash Mountain Complex, Sierra Nevada batholith, California (USA). Geosphere 9(4):691-717

Icenhower JP, London D (1997) Partitioning of fluorine and chlorine between biotite and granitic melt: experimental calibration at 200 MPa H 2 O. Contributions to Mineralogy and Petrology 127(1-2):17-29

Jagoutz O (2014) Arc crustal differentiation mechanisms. Earth and Planetary Science Letters 396:267-277

Jagoutz O, Klein B (2018) On the importance of crystallization-differentiation for the generation of SiO2-rich melts and the compositional build-up of arc (and continental) crust. American Journal of Science 318(1):29-63

Jagoutz OE (2010) Construction of the granitoid crust of an island arc. Part II: a quantitative petrogenetic model. Contributions to Mineralogy and Petrology 160(3):359-381

Jagoutz OE, Burg J-P, Hussain S, Dawood H, Pettke T, Iizuka T, Maruyama S (2009) Construction of the granitoid crust of an island arc part I: geochronological and geochemical constraints from the plutonic Kohistan (NW Pakistan). Contributions to Mineralogy and Petrology 158(6):739-755

Jones CH, Phinney RA (1998) Seismic structure of the lithosphere from teleseismic converted arrivals observed at small arrays in the southern Sierra Nevada and vicinity, California. Journal of Geophysical Research: Solid Earth 103(B5):10065-10090

Kay SM, Kay R (1985) Role of crystal cumulates and the oceanic crust in the formation of the lower crust of the Aleutian arc. Geology 13(7):461-464

Kelley KA, Cottrell E (2009) Water and the oxidation state of subduction zone magmas. Science 325(5940):605-607

Kirsch M, Paterson SR, Wobbe F, Ardila AMM, Clausen BL, Alasino PH (2016). Temporal histories of Cordilleran continental arcs: Testing models for magmatic episodicity. American Mineralogist, 101(10): 2133-2154.

Klein BZ, Jagoutz OE (2021) Construction of a trans-crustal magma system: Building the Bear Valley Intrusive Suite, southern Sierra Nevada, California. Earth and Planetary Science Letters, 553:116624

Köhler T, Brey G (1990) Calcium exchange between olivine and clinopyroxene calibrated as a geothermobarometer for natural peridotites from 2 to 60 kb with applications. Geochimica et Cosmochimica Acta 54(9):2375-2388

Krawczynski MJ, Grove TL, Behrens H (2012) Amphibole stability in primitive arc magmas: effects of temperature, H 2 O content, and oxygen fugacity. Contributions to Mineralogy and Petrology 164(2):317-339

Kress VC, Carmichael IS (1991) The compressibility of silicate liquids containing Fe2O3 and the effect of composition, temperature, oxygen fugacity and pressure on their redox states. Contributions to Mineralogy and Petrology 108(1-2):82-92

Lackey JS, Valley JW, Saleeby JB (2005) Supracrustal input to magmas in the deep crust of Sierra Nevada batholith: Evidence from high-δ18O zircon. Earth and Planetary Science Letters 235(1-2):315-330

Lackey, JS, Valley, JW, Chen, JH, Stockli, DF (2008). Dynamic magma systems, crustal recycling, and alteration in the central Sierra Nevada batholith: The oxygen isotope record. Journal of Petrology, 49(7):1397-1426

Leake BE, Woolley AR, Arps CE, Birch WD, Gilbert MC, Grice JD, Hawthorne FC, Kato A, Kisch HJ, Krivovichev VG (1997) Nomenclature of amphiboles; report of the subcommittee on amphiboles of the International Mineralogical Association, Commission on New Minerals and Mineral Names. The Canadian Mineralogist 35(1):219-246

Lee, C-TA, Bachmann, O (2014). How important is the role of crystal fractionation in making intermediate magmas? Insights from Zr and P systematics. Earth and Planetary Science Letters, 393:266-274

Lee C-TA, Cheng X, Horodyskyj U (2006) The development and refinement of continental arcs by primary basaltic magmatism, garnet pyroxenite accumulation, basaltic recharge and delamination: insights from the Sierra Nevada, California. Contributions to Mineralogy and Petrology 151(2):222-242

Lee C-T, Rudnick RL, Brimhall Jr GH (2001) Deep lithospheric dynamics beneath the Sierra Nevada during the Mesozoic and Cenozoic as inferred from xenolith petrology. Geochemistry, Geophysics, Geosystems 2(12)

Lockwood J, Bateman P (1976) Geologic map of the Shaver Lake 15-minute quadrangle, central Sierra Nevada, California: US Geological Survey. Geologic Quadrangle Map GQ-1271, scale 1(62,500)

Mason RA (1992) Models of order and iron-fluorine avoidance in biotite. Canadian Mineralogist 30(2):343-354

Mayo EB (1941) Deformation in the interval Mt. Lyell-Mt. Whitney, California. Bulletin of the Geological Society of America 52(7):1001-1084

McCarthy A, Müntener O (2016) Comb layering monitors decompressing and fractionating hydrous mafic magmas in subvolcanic plumbing systems (Fisher Lake, Sierra Nevada, USA). Journal of Geophysical Research: Solid Earth 121(12):8595-8621

Melekhova E, Blundy J, Robertson R, Humphreys MC (2015) Experimental evidence for polybaric differentiation of primitive arc basalt beneath St. Vincent, Lesser Antilles. Journal of Petrology 56(1):161-192

Middlemost EA (1994) Naming materials in the magma/igneous rock system. Earth-Science Reviews 37(3-4):215-224

Miller DM, Goldstein SL, Langmuir CH (1994) Cerium/lead and lead isotope ratios in arc magmas and the enrichment of lead in the continents. Nature 368(6471):514-520

Mukhopadhyay B (1991) Garnet breakdown in some deep seated garnetiferous xenoliths from the central Sierra Nevada: petrologic and tectonic implications. Lithos 27(1):59-78

Mukhopadhyay B, Manton W (1994) Upper-mantle fragments from beneath the Sierra Nevada Batholith: partial fusion, fractional crystallization, and

metasomatism in a subduction related ancient lithosphere. Journal of Petrology 35(5):1417-1450

Müntener O, Kelemen PB, Grove TL (2001) The role of H2O during crystallization of primitive arc magmas under uppermost mantle conditions and genesis of igneous pyroxenites: an experimental study. Contributions to Mineralogy and Petrology 141(6):643-658

Müntener O, Ulmer P (2018) Arc crust formation and differentiation constrained by experimental petrology. American Journal of Science 318(1):64-89

Mutch E, Blundy J, Tattitch B, Cooper F, Brooker R (2016) An experimental study of amphibole stability in low-pressure granitic magmas and a revised Al-in-hornblende geobarometer. Contributions to Mineralogy and Petrology 171(10):85

Nadin, ES, Saleeby, JB, Wong, M.(2016) Thermal evolution of the Sierra Nevada batholith, California, and implications for strain localization. Geosphere, 12(2):377-399

Nadin ES, Saleeby JB, Wright J, Shervais J (2008) Disruption of regional primary structure of the Sierra Nevada batholith by the Kern Canyon fault system, California. Geological Society of America - Special Papers 438:429

Nandedkar RH, Ulmer P, Müntener O (2014) Fractional crystallization of primitive, hydrous arc magmas: an experimental study at 0.7 GPa. Contributions to Mineralogy and Petrology 167(6):1015

Oliver TA (1951) The effect of uralitization upon the chemical composition of the Sudbury norite. American Mineralogist 36(5-6):421-429

Otamendi JE, Ducea MN, Bergantz GW (2012) Geological, petrological and geochemical evidence for progressive construction of an arc crustal section, Sierra de Valle Fertil, Famatinian Arc, Argentina. Journal of Petrology 53(4):761-800

Peselnick L, Lockwood JP, Stewart R (1977) Anisotropic elastic velocities of some upper mantle xenoliths underlying the Sierra Nevada batholith. Journal of Geophysical Research 82(14):2005-2010

Pickett DA, Saleeby JB (1993) Thermobarometric constraints on the depth of exposure and conditions of plutonism and metamorphism at deep levels of the Sierra Nevada batholith, Tehachapi Mountains, California. Journal of Geophysical Research: Solid Earth 98(B1):609-629

Piispanen R, Alapieti T (1977) Uralitization-an example from Kuusamo, Finland. Bulletin of the Geological Society of Finland 49(2):39-46

Portnyagin M, Hoernle K, Plechov P, Mironov N, Khubunaya S (2007) Constraints on mantle melting and composition and nature of slab components in volcanic arcs from volatiles (H2O, S, Cl, F) and trace elements in melt

inclusions from the Kamchatka Arc. Earth and Planetary Science Letters 255(1-2):53-69

Putirka KD (2008) Thermometers and barometers for volcanic systems. Reviews in mineralogy and geochemistry 69(1):61-120

Ratajeski K, Glazner AF, Miller BV (2001) Geology and geochemistry of mafic to felsic plutonic rocks in the Cretaceous intrusive suite of Yosemite Valley, California. Geological Society of America Bulletin 113(11):1486-1502

Reid Jr JB, Evans OC, Fates DG (1983) Magma mixing in granitic rocks of the central Sierra Nevada, California. Earth and Planetary Science Letters 66:243-261

Rezeau H, Klein BZ, Jagoutz O (2021) Mixing dry and wet magmas in the lower crust of a continental arc: New petrological insights from the Bear Valley Intrusive Suite, southern Sierra Nevada, California. Contributions to Mineralogy and Petrology

Ross DC (1985) Mafic: gneissic complex (batholithic root?) in the southernmost Sierra Nevada, California. Geology 13(4):288-291

Rowe MC, Kent AJ, Nielsen RL (2009) Subduction influence on oxygen fugacity and trace and volatile elements in basalts across the Cascade Volcanic Arc. Journal of Petrology 50(1):61-91

Ruppert S, Fliedner MM, Zandt G (1998) Thin crust and active upper mantle beneath the southern Sierra Nevada in the western United States. Tectonophysics 286(1-4):237-252

Saleeby J, Ducea MN, Busby C, Nadin E, Wetmore PH, Wright J, Shervais J (2008) Chronology of pluton emplacement and regional deformation in the southern Sierra Nevada batholith, California. Geological Society of America - Special Papers 438:397

Sams DB, Saleeby JB (1988) Geology and petrotectonic significance of crystalline rocks of the southernmost Sierra Nevada, California, in WG Ernst, Metamorphism and Crustal Evolution of the Western United States (Rubey Volume 7): Prentice Hall Inc 865:893

Schmidt MW, Jagoutz O (2017) The global systematics of primitive arc melts. Geochemistry, Geophysics, Geosystems 18(8):2817-2854

Sisson T, Grove T (1993) Experimental investigations of the role of H 2 O in calc-alkaline differentiation and subduction zone magmatism. Contributions to Mineralogy and Petrology 113(2):143-166

Sisson T, Grove T, Coleman D (1996) Hornblende gabbro sill complex at Onion Valley, California, and a mixing origin for the Sierra Nevada batholith. Contributions to Mineralogy and Petrology 126(1-2):81-108

Sisson T, Layne G (1993) H2O in basalt and basaltic andesite glass inclusions from four subduction-related volcanoes. Earth and Planetary Science Letters 117(3-4):619-635

Sisson T, Ratajeski K, Hankins W, Glazner AF (2005) Voluminous granitic magmas from common basaltic sources. Contributions to Mineralogy and Petrology 148(6):635-661

Soesoo A (2000) Fractional crystallization of mantle-derived melts as a mechanism for some I-type granite petrogenesis: an example from Lachlan Fold Belt, Australia. Journal of the geological Society 157(1):135-149

Sparks R, Marshall L (1986) Thermal and mechanical constraints on mixing between mafic and silicic magmas. Journal of volcanology and Geothermal Research 29(1-4):99-124

Stolz A, Jochum K, Spettel B, Hofmann A (1996) Fluid-and melt-related enrichment in the subarc mantle: evidence from Nb/Ta variations in island-arc basalts. Geology 24(7):587-590

Sun, S. S., & McDonough, W. F. (1989). Chemical and isotopic systematics of oceanic basalts: implications for mantle composition and processes. Geological Society, London, Special Publications, 42(1), 313-345

Ulmer P, Kaegi R, Müntener O (2018) Experimentally derived intermediate to silica-rich arc magmas by fractional and equilibrium crystallization at 1· 0 GPa: an evaluation of phase relationships, compositions, liquid lines of descent and oxygen fugacity. Journal of Petrology 59(1):11-58

Vermeesch P (2018) IsoplotR: A free and open toolbox for geochronology. Geoscience Frontiers 9(5):1479-1493

Villiger S, Ulmer P, Müntener O, Thompson AB (2004) The liquid line of descent of anhydrous, mantle-derived, tholeiitic liquids by fractional and equilibrium crystallization—an experimental study at 1· 0 GPa. Journal of Petrology 45(12):2369-2388

Walker BA, Bergantz GW, Otamendi JE, Ducea MN, Cristofolini EA (2015) A MASH zone revealed: the mafic complex of the Sierra Valle Fértil. Journal of Petrology 56(9):1863-1896

Waters LE, Lange RA (2015) An updated calibration of the plagioclase-liquid hygrometer-thermometer applicable to basalts through rhyolites. American Mineralogist 100(10):2172-2184

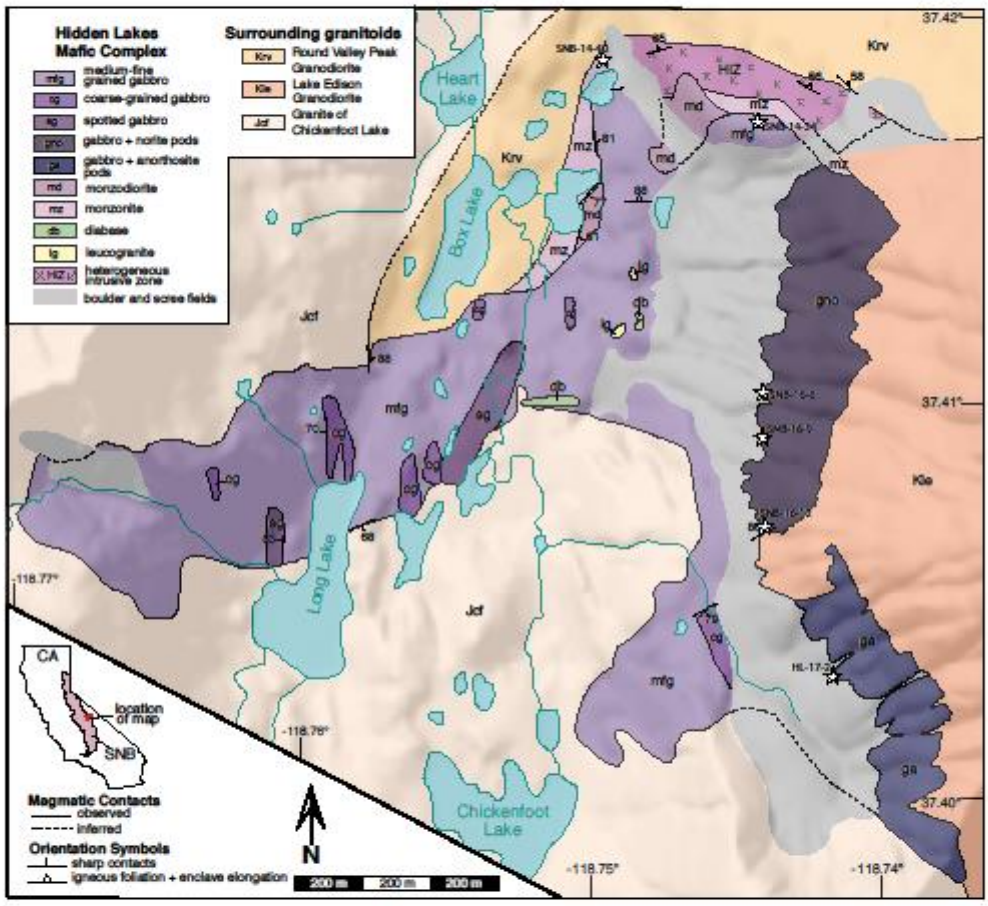
Hidden Lakes Mafic Complex
mfg medium-fine grained gabbro
cg coarse-grained gabbro
sg spotted gabbro
gno gabbro + norite pods
ga gabbro + anorthosite pods
md monzodiorite
mz monzonite
db diabase
lg leucogranite
HIZ heterogeneous intrusive zone
boulder and scree fields
Surrounding granitoids
Krv Round Valley Peak Granodiorite
Kle Lake Edison Granodiorite
Jcf Granite of Chickenfoot Lake
Heart Lake
Box Lake
Long Lake
Chickenfoot Lake
37.42°
37.41°
37.40°
-118.77°
-118.76°
-118.75°
-118.74°
CA
location of map
SNB
Magmatic Contacts
observed
inferred
Orientation Symbols
sharp contacts
igneous foliation + enclave elongation
N
200 m
200 m
200 m

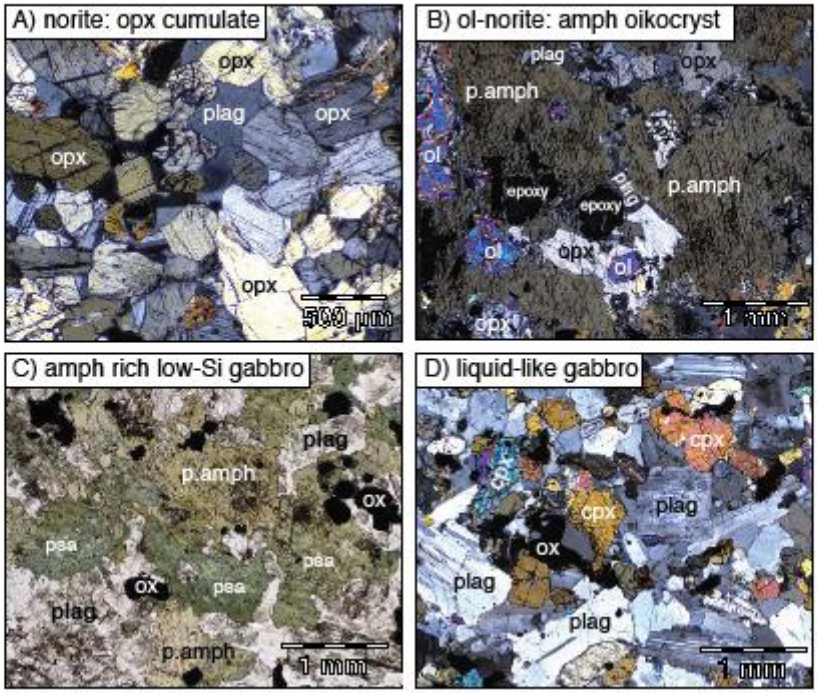
A) norite: opx cumulate
opx
plag
opx
opx
opx
500 µm
B) ol-norite: amph oikocryst
plag
opx
p.amph
ol
epoxy
epoxy
p.amph
ol
opx
ol
opx
1 mm
C) amph rich low-Si gabbro
plag
p.amph
ox
psa
psa
ox
psa
plag
p.amph
1 mm
D) liquid-like gabbro
cpx
cpx
cpx
plag
ox
plag
plag
1 mm

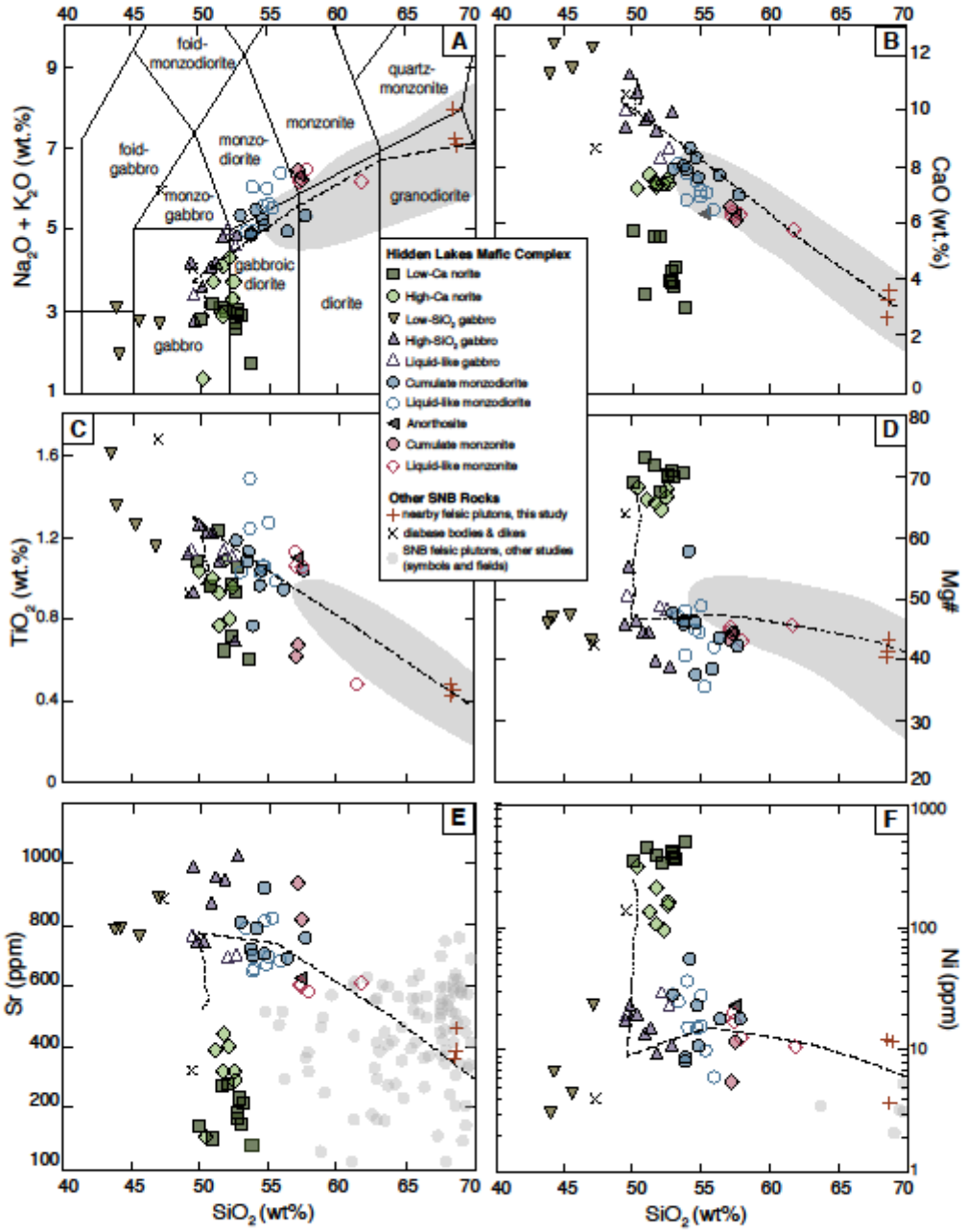

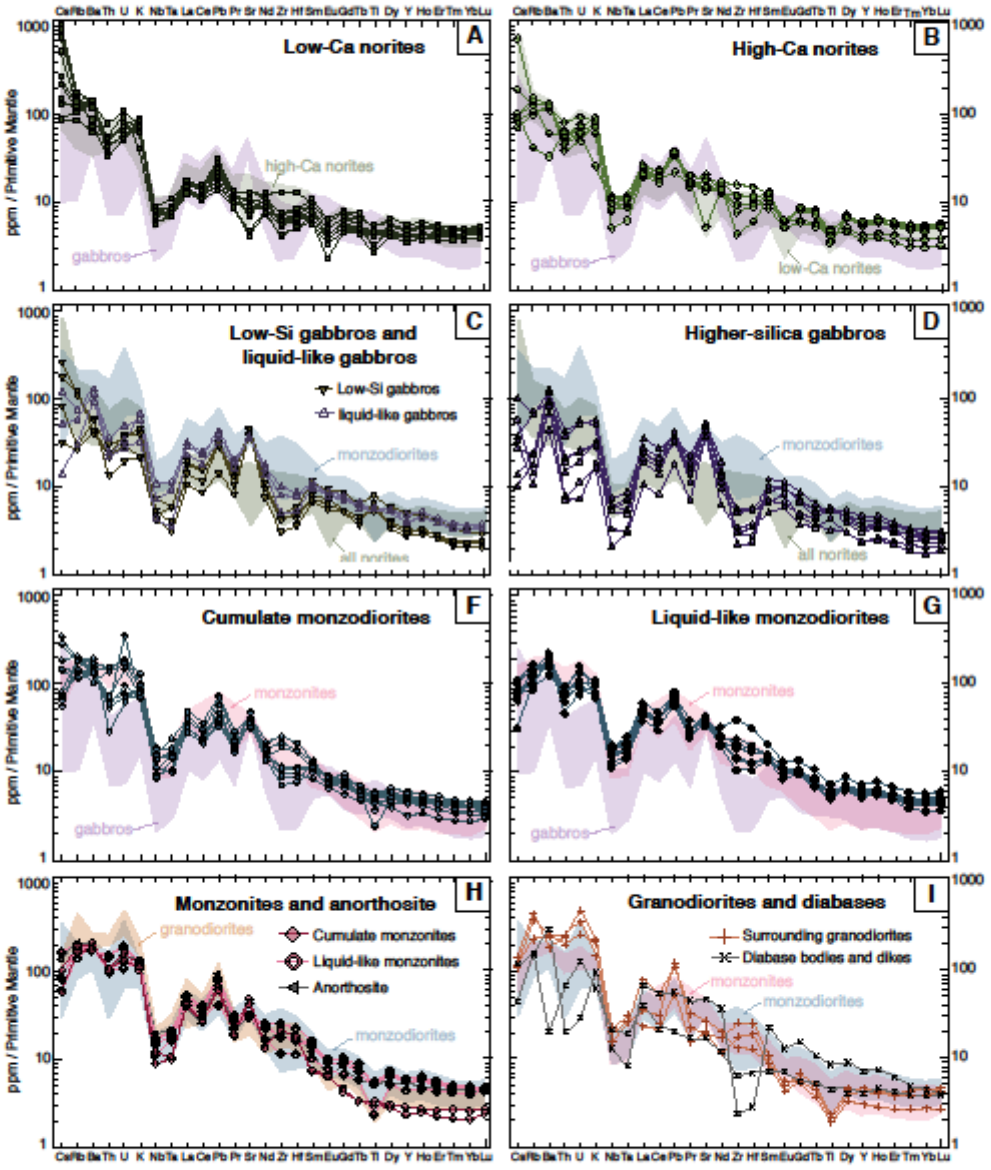
Low-Ca norites
A
high-Ca norites
gabbros
High-Ca norites
B
gabbros
low-Ca norites
Low-Si gabbros and liquid-like gabbros
C
Low-Si gabbros
liquid-like gabbros
monzodiorites
Higher-silica gabbros
D
monzodiorites
all norites
Cumulate monzodiorites
F
monzonites
gabbros
Liquid-like monzodiorites
G
monzonites
gabbros
Monzonites and anorthosite
H
granodiorites
Cumulate monzonites
Liquid-like monzonites
Anorthosite
monzodiorites
Granodiorites and diabases
I
Surrounding granodiorites
Diabase bodies and dikes
monzonites
monzodiorites
ppm / Primitive Mantle
1000
100
10
1

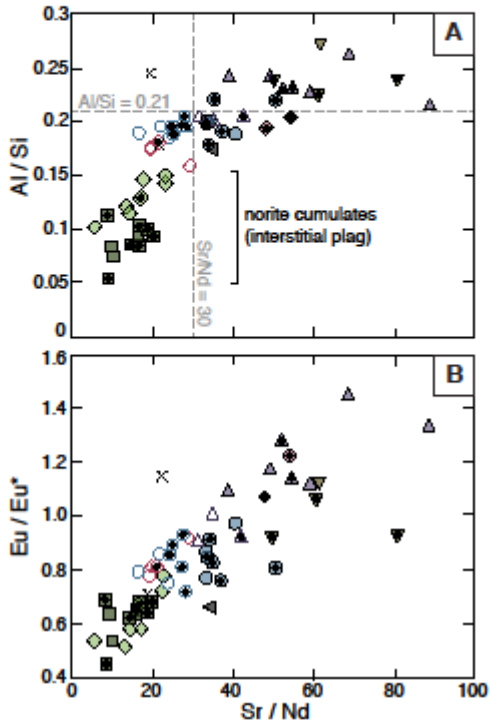

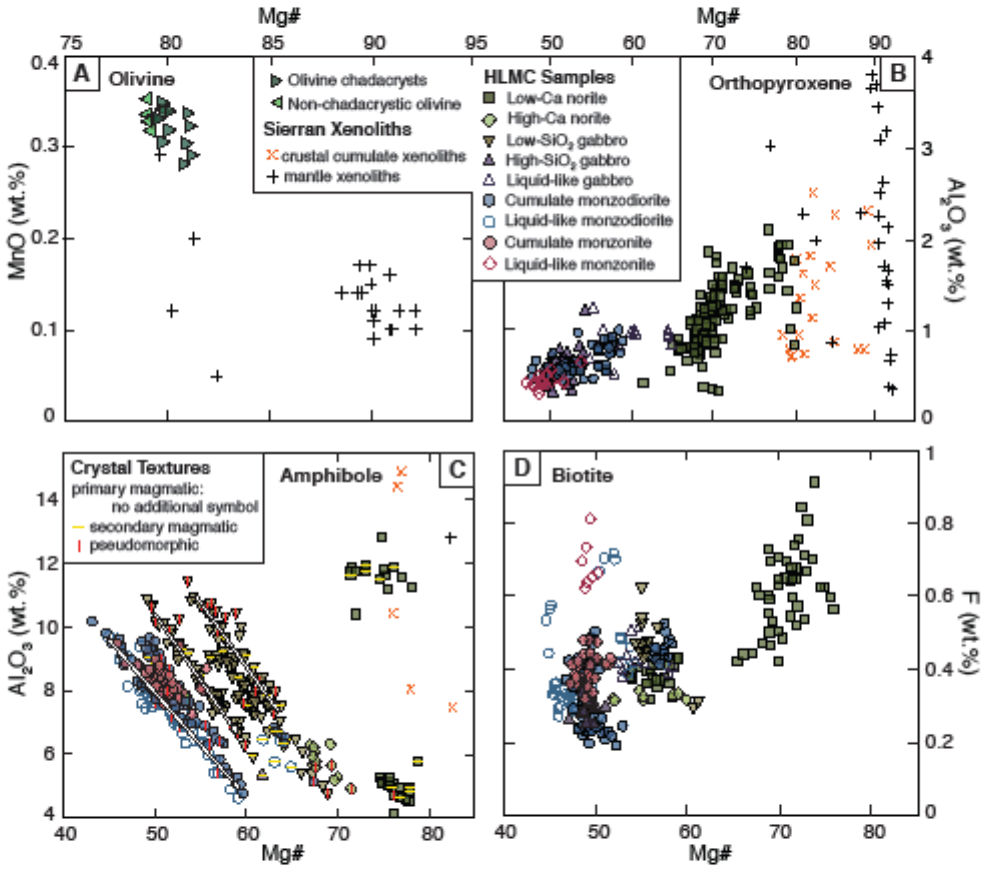

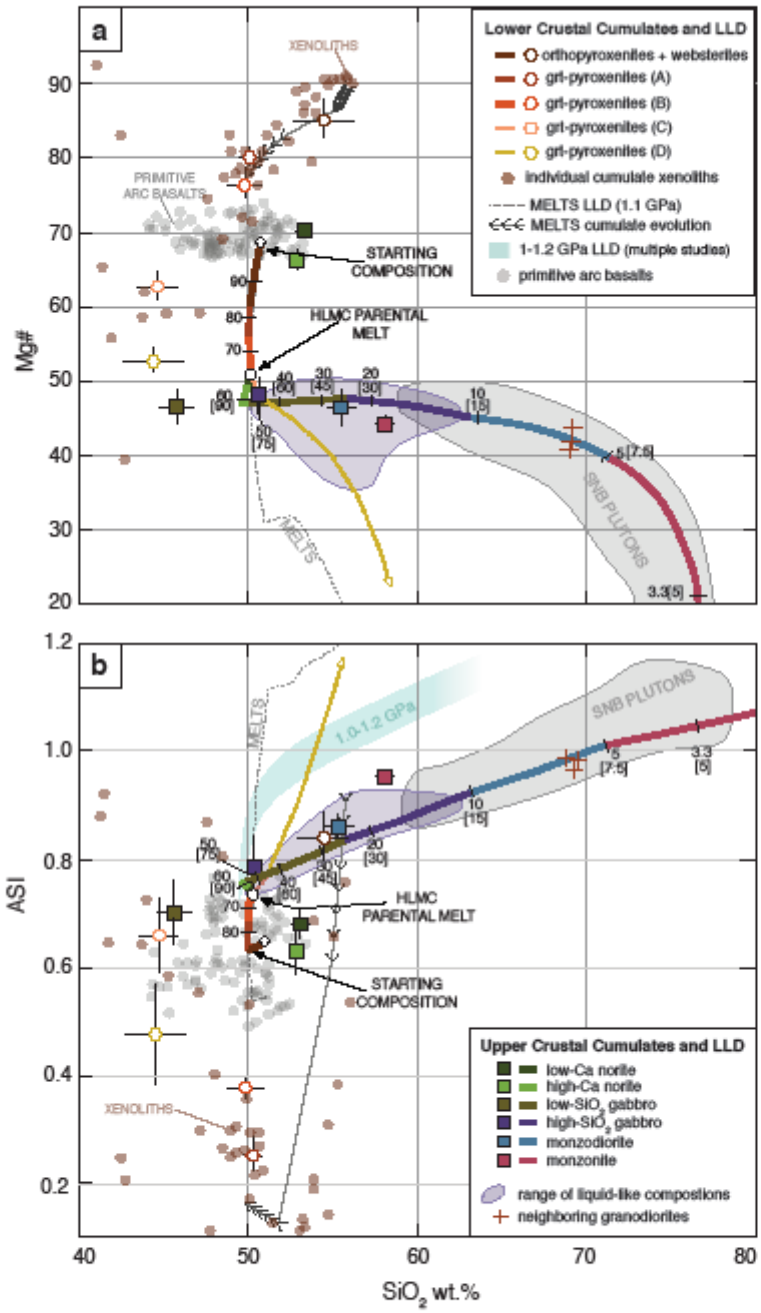

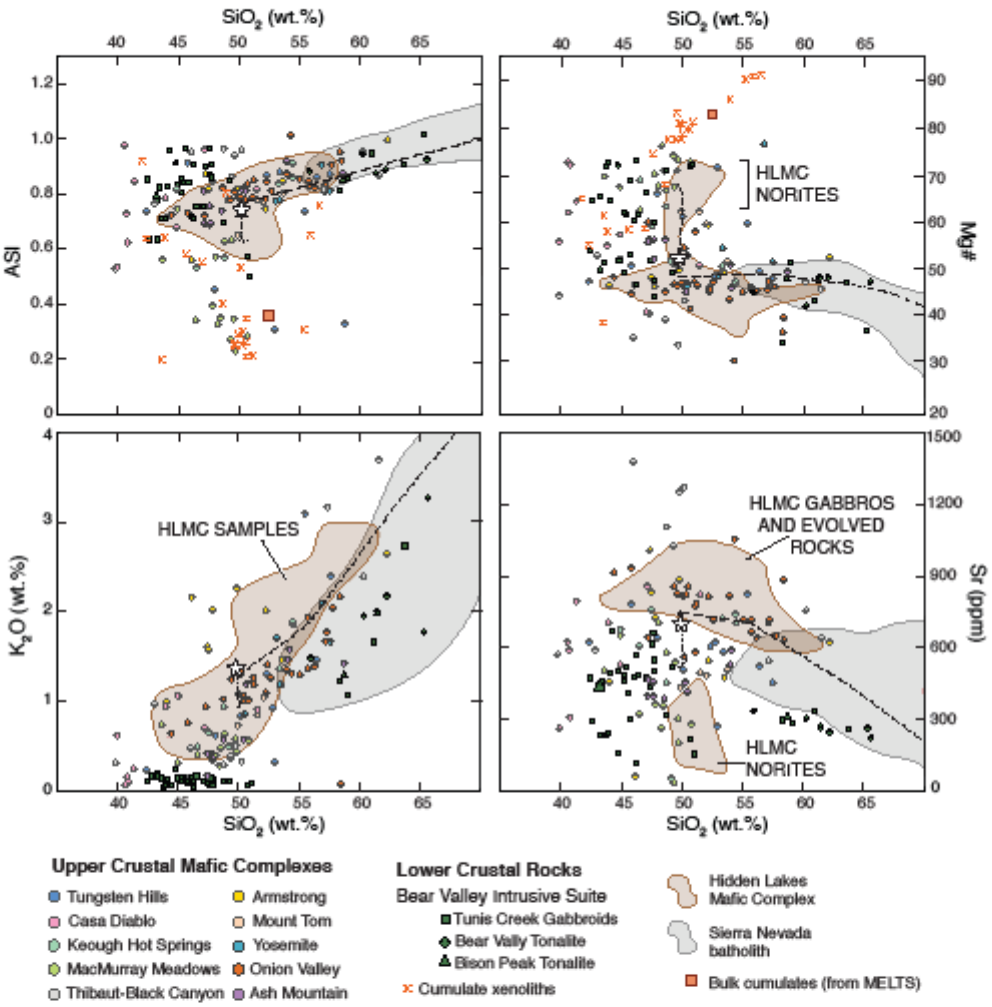

Table 1: Summary of Modal Mineralogies

	norite	gabbro (coarse-grained)	gabbro (medium-fine grained)	monzodiorite	monzonite	anorthosite
olivine	0-<1[a]	–	–	–	–	–
orthopyroxene	15-75	–	~5	–	0-<1	–
clinopyroxene	1-5	5-20	5-15	0-2	0-<1	–
plagioclase	15-40	45-70	65-75	60-70	40-60	90-95
amphibole	0-20	25-50	5-20	5-15	0-5	–
biotite	5-15	5-10	5-10	15-20	10-20	5-10
K-feldspar	0-<1	<1	<1	10-15	20-35	–
quartz	–	–	–	0-2	0-5	–

[a] all modal mineralogies are given in percent and estimated visually, with ranges reflecting variability within each lithologic group. Uncertainties are roughly 10% of reported values.

Table 2: Calculated Crystallization Conditions

	Method	norites	gabbros	monzodiorites	monzonites
Temperature (°C)	Ca-in-opx[a]	900- 1170	930- 1100	970- 1030	850- 1010
	plag-amph pairs[b]	865- 950 (oikocrysts)	740- 815 (magmatic amph)	815- 870	800- 850
		700- 765 (non-oikocrystic)	1040-1120 (pseudomorphic amph)		
Pressure (GPa)	Al-in-amph[c]	[0.32][f]	[0.32]	[0.32]	0.32
H_2O (wt.%)	plag hygrometry[d]		2.9- 3.5		6-7
fO_2 (ΔNNO, ±1 log unit)	biotite[e]				0-0.6

[a] Method of Köhler and Brey (1990)
[b] Method of Blundy and Holland (1990)
[c] Method of Mutch et al. (2016)
[d] Method of Waters and Lange (2015)
[e] Method of Bucholz et al. (2018)
[f] Values in brackets indicate those that were not calculated from that particular rock type due to mineral assemblage constraints, but are assumed to be constant throughout the fractionation sequence (e.g. pressure and fO_2)